



Comparison of embryonic and adult shells of *Sepia officinalis* (Cephalopoda, Mollusca)

Yannicke Dauphin, Gilles Luquet, Aline Percot, Laure Bonnaud-Ponticelli

► To cite this version:

Yannicke Dauphin, Gilles Luquet, Aline Percot, Laure Bonnaud-Ponticelli. Comparison of embryonic and adult shells of *Sepia officinalis* (Cephalopoda, Mollusca). *Zoomorphology*, 2020, 139 (2), pp.151-169. 10.1007/s00435-020-00477-2 . hal-02557254

HAL Id: hal-02557254

<https://hal.science/hal-02557254>

Submitted on 28 Apr 2020

HAL is a multi-disciplinary open access archive for the deposit and dissemination of scientific research documents, whether they are published or not. The documents may come from teaching and research institutions in France or abroad, or from public or private research centers.

L'archive ouverte pluridisciplinaire **HAL**, est destinée au dépôt et à la diffusion de documents scientifiques de niveau recherche, publiés ou non, émanant des établissements d'enseignement et de recherche français ou étrangers, des laboratoires publics ou privés.

[Click here to view linked References](#)

Comparison of embryonic and adult shells of *Sepia officinalis* (Cephalopoda, Mollusca)

Yannicke Dauphin^{1,*}, Gilles Luquet², Aline Percot³, Laure Bonnaud-Ponticelli^{2,*}

¹Institut de Systématique, Evolution, Biodiversité, UMR 7205 CNRS, Sorbonne Université, EPHE, Muséum National d'Histoire Naturelle, Paris, France & Department of Biomaterials, Max-Planck-Institute of Colloids and Interfaces, Potsdam, Germany

²Biologie des Organismes et Ecosystèmes Aquatiques, UMR CNRS 7208, Sorbonne Université, IRD 207, UCN, UA, Muséum National d'Histoire Naturelle, Paris, France

³De la Molécule aux Nano-Objets: Réactivité, Interactions et Spectroscopies, UMR 8233 CNRS, Sorbonne Université, Paris, France

*Corresponding authors

Yannicke Dauphin, yannicke.dauphin@upmc.fr, ORCID: 0000-0003-2870-8409

Laure Bonnaud-Ponticelli, laure.bonnaud@mnhn.fr, ORCID: 0000-0001-7510-5032

Abstract

Development and evolution of the shell in cephalopods is difficult to establish as there is few species with a calcified shell that could be fossilized (stable in geological time). Internal cuttlebone of sepiids is so particular that homologies are difficult to find. The developmental sequence in embryos give some response elements by comparison with adult cuttlebone. The macro and microstructure of adult shell is well known but an approach at nanostructural level allows to determine structure and composition of the two main parts, the dorsal shield and chambered part. We evidence in the embryonic shell, mainly organic, a light calcification of the shell, which occurs directly as aragonite, as it is all along the formation of the shell and whatever the parts. In embryonic shell, the prismatic and/or lamellar layers, present in adult, are not differentiated and the dorsal shield grows progressively, from posterior to anterior. Despite microstructural differences, all layers of both chambered part and dorsal shield are composed of rounded nanogranules (between 50 and 100 nm), similar to what is found in other mollusc shells. Finally, the presence of pillars evidenced in embryo suggests either that their absence in extinct

lineages of sepiids is the result of a diagenetic process or that they are a novelty in present sepiid species.

Keywords *Sepia* – embryonic shell - structure - composition

Introduction

Mollusks are a major group of marine organisms. Among them, cephalopods received a peculiar attention in different fields of research. They are able to synthesize inner or outer shells and are consequently of interest in biomineralization (Mutvei 1964; Dauphin 1979, 1981; Lowenstam and Weiner 1989; Bandel 1990; Marie et al. 2009; Cuif et al. 2013; Checa et al. 2015; Le Pabic et al. 2016) as well as from an evolutionary point of view (Haas 2003; Kröger et al. 2011; Allcock et al. 2015). Known since the Paleozoic era, they are used in palaeontology as good stratigraphic markers because of calcified shells, fast evolution and large dispersion of major extinct species. Only three extant cephalopod genera are able to build a calcified shell: external in *Nautilus*, internal in *Spirula* and *Sepia*. For this particularity, they are used in biomimetic and biomedical research (Ogasawara et al. 2000; Kim et al. 2012; Karthika et al. 2016). Recently, calcified processes have been studied in the context of global change and ocean acidification (Gutowska et al. 2008; Dorey et al. 2013; Sigwart et al. 2015).

Sepia officinalis Linnaeus, 1758 and *Sepia pharaonis* Ehrenberg, 1931 are the most studied species, notably because of their abundance and commercial interest as seafood (Bettencourt and Guerra 2001; Sykes et al. 2014).

One of the first detailed microstructural analyses of the shell and the living tissues of *Sepia officinalis* was that of Appellöf (1893). The proostracum (dorsal shield component), the ventral part with pillars and lamellae, the fork, the siphonal tube and the rostrum were identified by Naef (1922). The continuity of the layers in dorsal shield and rostrum was described, as well as the presence of chitin (Appellöf 1893; Naef 1922). Numerous comparative studies have been done to establish homologies of the different parts of the shell of present versus fossil coleoids. In his comprehensive work on the structure and mineralogy of mollusc shells, Boggild (1930) noted that the dorsal shield is composed of three layers, the median layer being fully organic in

1
2
3
4 the lateral part, and more or less calcified in the middle of the cuttlebone. He also showed that all
5 the layers of *Sepia* are aragonitic, the dorsal shield and the rostrum being prismatic. As other
6 cephalopod shells, the aragonite has a low Sr content (Dauphin et al. 2007; Florek et al. 2009).
7
8 The structure of the chambered part and the labyrinthine (“meanderlike”) organization of the
9 pillars/walls were also described and illustrated. Barskov (1973) used SEM to observe the minute
10 structure of the cuttlebone and described the microstructure of the septa. A comparison of some
11 *Sepia* species has shown that despite differences in the morphology of the cuttlebone, their
12 arrangements and microstructures are similar (Dauphin 1981). The regular layered structure of
13 the septa of *Spirula* was described by Grégoire (1961, 1967), who called it “nacre” despite the
14 absence of tablets. The same structure was also called “lamellar fibrillar structure” (Erben 1972)
15 or “type II nacre” (Mutvei 1970), then lamello-fibrillar nacre (Mutvei 2016). Such a structure
16 was also found in *Sepia* (Dauphin and Keller 1982; Doguzhaeva and Dunca 2015).
17
18
19
20
21
22
23
24
25

26 Recently an analysis of the cuttlebone using for the first time CT-scan has drawn a
27 dynamic 3D image of the development and growth of the shell from embryo to adult (Le Pabic et
28 al. 2019).
29
30
31

32 Most studies dealing with the microstructure and composition of the cuttlebones were
33 performed on adult samples. For example, the presence of chitin and proteins in the adult
34 cuttlebone has been shown by Degens et al. (1967), Drozdova et al. (1971), Hunt and Nixon
35 (1981).
36
37
38

39 The first studies on embryonic shell of *S. officinalis* and *S. pharaonis* were done by
40 Bandel and Boletzky (1979), then detailed by Sen (2013) and Le Pabic et al. (2016, 2019), but
41 the microstructures and compositions of the calcified parts of *Sepia* embryonic shells remained
42 to be more accurately characterized.
43
44
45

46 In this study, we therefore examined the microstructures and nanostructures of the
47 calcified parts of *Sepia officinalis* embryonic shells, with some data on their composition, in
48 comparison to the adult cuttlebone and other mineralized structures synthesized by mollusks. In
49 addition to the understanding of variation in building the shell during development and growth of
50 animal, our study brings new information on shell evolution within mollusks.
51
52
53
54
55
56
57
58
59
60
61
62
63
64
65

Material and methods

Materials

Sepia officinalis adult shells were collected on beaches in Normandy (France). The maximal length of the cuttlebones was 30 cm.

S. officinalis eggs were collected in Luc-sur-Mer (Normandie, France) and kept in the lab in artificial sea water (salinity: 35 ppt - closed circulatory system), at 18°C. Eggs were opened and the embryos (whose stage is determined by morphological characteristics) were immersed in sea-water with 5% Ethanol, following recommendations of Buttler-Struben et al. (2018) and Winlow et al. (2018) and according to directive 2010-63-UE and French decree 2013-118. Cuttlebones were obtained by dissection. All soft tissues were removed and the cuttlebones were kept dried.

Naef (1922, 1928a, 1928b) has divided the embryonic period into stages, specified later by Lemaire (1970) and Boletzky et al. (2016). We used the Lemaire and Boletzky et al. staging in this study. Stages from the beginning of matrix shell formation (stage 24), beginning of mineralisation (and first chamber, stage 25) to early final stage 30 (6 to 8 chambers) were analysed.

Crab chitin (Sigma Aldrich) and Bovine serum albumin (BSA, Eurobio) were used as references for the organic components. A marine non biogenic aragonite (botryoidal aragonite) was selected as a mineral reference.

Scanning electron microscopy (SEM)

A Philips XL30 and a Zeiss Gemini LEO 1550 were used on coated samples. Secondary electron images are indicated as SE–SEM in the legends. A FEI FESEM Quanta F600 and a Phenom Pro X were used for images in back scattered electron mode (BSE–SEM). In this technique, imaging contrast depends on the atomic number of the atoms composing the substrate material: the organic structures appear in black, in contrast to the mineral units with heavier chemical elements (Ca, Sr). The sample does not need to be covered by a conductive layer, so that the same sample can be used for SEM and AFM observations.

Fractured shells and polished samples were observed. Samples embedded in resin were

1
2
3
4 polished using various grades of diamond paste down to a final 0.25 mm grade. The polished
5
6 surfaces were then cleaned with a detergent mixed with hot water for 1 min under ultrasonication
7
8 to remove any oil residue from the pastes and rinsed with water. Then, according to the
9
10 technique subsequently employed, additional preparative procedures were undertaken, the details
11
12 of which are given in the figure captions.

13
14 Figure S1 displays the used terminology for the orientation of the sections.

15 16 17 **Atomic Force Microscopy (AFM)**

18
19
20 Samples were studied using a Nanoscope IIIa multi-mode scanning probe microscope operating
21
22 in tapping mode. The tapping mode AFM utilizes an oscillating tip with amplitude of
23
24 approximately several tens of nm when the tip is not in contact with the surface. The resolution
25
26 of tapping mode AFM is in the order of a few nm. Phase imaging is a powerful extension to
27
28 detect variations in chemical composition, friction and other physical properties. The AFM
29
30 sensor oscillates over the surface sample, and the amplitude of the oscillation is used to control
31
32 the scanner. An image can be formed from this amplitude signal that emphasizes the details of
33
34 the sample surface.

35
36 Compared with conventional secondary electron imaging SEM (SE-SEM), AFM
37
38 provides topographic direct height measurements and views of surface features since no coating
39
40 is necessary. Moreover, three-dimensional nanoscale resolution AFM images are obtained
41
42 without the time-consuming sample preparation (e.g. decalcification, thinning...) required for
43
44 similar resolution Transmission Electron Microscopy examination.

45 46 47 **Fourier Transform Infrared Spectrometry (FTIR)**

48
49
50 All spectra were recorded at 4 cm⁻¹ resolution with 16 scans on a Perkin-Elmer Frontier Fourier
51
52 transform infrared spectrometer (FTIR), in the wavenumber range 4000 to 450 cm⁻¹. The
53
54 spectrometer was equipped with a Diffuse Reflectance accessory, which permits DRIFT
55
56 measurements with high sensitivity on powders. All spectra were corrected by the Kubelka-
57
58 Munk function. A background spectrum was measured for pure KBr. Sample spectra were
59
60 automatically ratioed against background to minimize CO₂ and H₂O bands. Correlation
61
62
63
64
65

coefficients between two spectra of the same samples were about 99%. The dorsal shield and the ventral zone were mechanically separated in adult samples, immersed in 3% NaClO for 1 h to remove organic contaminants, rinsed with Milli-Q water, dried, and ground into powder.

Micro-Raman spectroscopy

The Raman spectra were recorded with a LabRam HR 800 spectrometer (Horiba Jobin Yvon) equipped with a Peltier cooled CCD detector and using the 514 nm line of a water-cooled Ar⁺ laser (Innova 90C, Coherent Inc.). Raman scattering is collected via a microscope (Olympus) equipped with a 50x long working distance objective, allowing a laser spot size of about 5 µm. The laser power at the sample is between 2 and 3 mW. The spectrometer is equipped with a 600 lines/mm grating and allowing a 2 cm⁻¹ spectral resolution on the range 100-1700 cm⁻¹. Calibration has been checked with respect to the 520.7 cm⁻¹ band of silicon. Typical recording times consist of 3 accumulations of 10 s.

Calcein labelling

Stage 25/26 and 30 embryos were incubated *in vitro* in calcein-containing seawater (30 mg/L; CNAM, Sigma) during 24h followed by 48h incubation in seawater without dye. Then shells were removed from frozen embryos and observed using a Leica DM-IRB microscope.

Results

Morphology - terminology

The descriptive terminology of the cuttlebone and the comparisons with external shells differ according to the authors. Here, we used the main terms defined by Barskov (1973). The adult cuttlebone is divided into two main parts: the compact dorsal shield and the porous ventral zone, called chambered part (Fig. 1A). The ventral zone contains the septa, the siphuncular zone and the fork (Fig. 1A); the posterior part of the cuttlebone is sharp and called rostrum or spine (Fig. 1B). In embryo, the dorsal shield is thin, and thanks to transparency, the complex outlines of the

1
2
3
4 first septa are visible (Fig. 1C). The growth occurs anteriorly by a ventral addition of new septa,
5
6 delimitating chambers sustained by pillars, all being slightly mineralized (Fig. 1D-F). The fork,
7
8 wings and rostrum are absent in the embryo cuttlebones (Fig. 1C, D). At hatching, the shell is
9
10 composed of 6 to 8 chambers (Fig. 1F).

11
12 The organization of the adult cuttlebone has been repeatedly described, so that only the
13
14 main features are here shown. The microstructure and nanostructure are detailed and illustrated.

15 16 17 **Dorsal shield (= outer wall)**

18 19 *Adult shell*

20
21 Three main layers are present in the dorsal shield (Fig. 2A, B): a thick prismatic outer spherulitic
22
23 layer, a layered median layer (type II nacre or lamello-fibrillar nacre) and a thin prismatic inner
24
25 layer. The outer spherulitic prismatic layer is composed of several sublayers (Fig. 2A, B). The
26
27 thickness of the sublayers is irregular, because of the spherulites seen on the outer surface and
28
29 described as tubercles (Appellöf 1893). Growth layers are visible, made of elongated crystallites
30
31 perpendicular to the sublayers (Fig. 2C). Etched and polished surfaces show the small diameter
32
33 ($< 1 \mu\text{m}$) of the crystallites of the outer layer, so that they are more acicular than prismatic (Fig.
34
35 2D-E). Unetched oblique fractures in these acicular crystallites show the non-geometric shapes
36
37 of granules (50-100 nm diameter) (Fig. 2F). The surface of the growth layers of the spherulitic
38
39 prismatic layer reveals that the granules are not adjacent (Fig. 2G), and the large content of
40
41 organic components is shown by AFM phase image contrast, as homogenous dark “flat” zones
42
43 (Fig. 2H). The shades of colour in AFM phase image within a granule are indicative of a
44
45 heterogeneous composition (Fig. 2I).

46
47 The median layer is thinner and shows overlapped sheets. The orientation of the acicular
48
49 crystallites differs in every sheet (Fig. 3A). A cross-section shows that the sheets are stacked,
50
51 parallel and thin (Fig. 3B, C) and some substructures perpendicular to the sheets are visible (Fig.
52
53 3C, stars). AFM height images show that a sheet is composed of rounded granules (Fig. 3D, E),
54
55 and that the granules have a heterogeneous composition, as shown by shades of colour in phase
56
57 contrast image (Fig. 3F).

58
59 The inner layer is prismatic and thin (Fig. 3G). Elongated crystallites are more or less
60
61 divergent towards the ventral side of the shell (Fig. 3G). At larger magnifications, granules are
62
63
64
65

1
2
3
4 irregular and do not seem aligned (Fig. 3H). They are composite (Fig. 3I), as shown by AFM
5 phase image.
6
7

8 9 *Embryonic shell*

10 The embryonic dorsal shield begins to be organized and grows from posterior to anterior.

11
12 At stage 24, the shell is still organic and the mineralization, even low, starts at stage 25 (Fig. 4A
13 and see below, Raman analysis). At stage 27, the thickness of the dorsal shield is about 15
14 microns (Fig. 4B-C). The prismatic structure of the outer layer (OP) is not well defined (Fig.
15 4D), and the elongated crystallites are not distinct (Fig. 4D). No sublayer is visible. The median
16 layer seems to be entirely organic (Fig. 4E) and no inner arrangement is evidenced. The inner
17 layer, IP, is similar to the outer layer, OP (Fig. 4D), with a somewhat indistinct arrangement.
18 Nevertheless, in some samples (the oldest one, i.e. stage 30), the elongated crystallites
19 perpendicular to the boundary of the layer are visible (Fig. 4E, F), so that this layer is said to be
20 prismatic. AFM phase images of the dorsal shield show rounded granules, and parallel elongated
21 structures (Fig. 4G). Elongated structures are composed of several parallel units, the diameter of
22 each one rangin4 from 20 to 50 nm (Fig. 4H). In the three layers of the dorsal shield, similar
23 rounded granules are present. They are surrounded by a cortex, as shown by amplitude, phase
24 and height images (Fig. 4I-K, c). In phase image (Fig. 4J), the cortex is darker than the inner part
25 of the granules, so that it contains more organic components. The presence of amorphous
26 calcium carbonate cannot be excluded. The maximal observed diameter of the granules is about
27 100 nm.
28
29
30
31
32
33
34
35
36
37
38
39
40
41

42 If the adult dorsal shield comprises three layers, at stages 27-30 the layers and structures
43 are not very distinct. At stage 28, near the growing edge and on the lateral parts of the dorsal
44 surface, a banding pattern of about 40-50 microns (Fig. 5A, B) and another one with thinner
45 growth lines are present (Fig. 5C). The first tubercles resulting from the irregular thickness of the
46 growth layer of the dorsal shield are visible (Fig. 5D). The posterior limit of every septum
47 corresponding to the aperture is easily identified on the ventral face (Fig. 5E-G). The most
48 posterior is a circular aperture corresponding to the open siphuncle (Fig. 5G).
49

50 After 24h *in vitro* incubation of the embryo in a calcein-containing sea water, and
51 observations using light and fluorescence microscopy, the progressive antero-posterior
52
53
54
55
56
57
58
59
60
61
62
63
64
65

development of the shield covering progressively the growing septum by irregular waves (Fig. 5 H-K) is well visible as well as the development of the pillars in each chamber (Fig. 5 I-K).

Ventral zone: chambered zone, septa

Adult shell

The ventral zone is porous. Longitudinal sections show parallel septa on which vertical pillars are inserted (Fig. 6A, Fig. S2A) so that chambers are reinforced. Pillars are covered by an organic membrane (Fig. 6B, C, m) with extensions parallel to the septa (Fig. 6B). In the adult chambers, minor growth zones are visible on the pillars (Fig. 6D, E). When the organic membranes on the surface of the pillars are removed, a granular structure is revealed, the granules being more or less arranged in columns (Fig. 6F, Fig. S2B). The average diameter of the granules is about 50 nm (Fig. 6G). Fractures parallel to the long axis or perpendicular to this axis show that pillars are not homogenous structures: the central part is hollow or soft (Fig. S2C, D).

Septa are composed of two layers (Fig. 6B, 6H: L). A closer examination shows a thin prismatic layer with crystallites perpendicular to the septa, and a lamello-fibrillar nacreous layer (Fig. 6C, H-I). Sections of the lamello-fibrillar nacre of the lamellae show the parallel arrangement of the superimposed sheets and lamellae seem to be well mineralized (Fig. 6J). The lamello-fibrillar nacre is composed of overlapped sheets and the orientation of acicular crystallites differs in two successive sublayers (Fig. 6K-L). The structure of the thin prismatic layer is similar to that of the inner layer of the dorsal shield.

Embryonic shell

As for the dorsal shield, the chambered part is not fully calcified so that the detailed structure is difficult to decipher. The outlines of septa are emphasized by the presence of more or less calcified zones, as shown by BSE images (Fig. 5E-G).

Septa comprise two parts: the pillars, perpendicular to the outer surface of the shell, and thin lamellae parallel to the outer surface of the shell. Pillars are not arranged in walls as in the adult shell, but they are isolated and their outline shows multiple folds (Fig. 7A, B). At the insertion of a pillar on a lamella, the basal part of the pillar is enlarged (Fig. 7C). Pillars are often branched (Fig. 7D, E, Fig. S2E). The surface of the lamellae between the pillars shows small granules (Fig. 7F, Fig. S2F). They are probably covered by a thin organic membrane, but no

horizontal extensions are present. The pillars are composed of successive growth layers (Fig. 7D, E), and transverse sections show that the outer peripheral layer is more calcified (Fig. 7F).

The septum building starts with the secretion of a chitinous layer visible on the edge of the ventral zone (Fig. 5F, star). Lamellae on which pillars are inserted are composed of two layers, a prismatic layer and a lamello-fibrillar nacre, as observed in adult (Fig. 7G, H: L). The insertion of a septum on the dorsal shield in an embryonic shell does not show distinct structures (Fig. 7I). The two layers of the lamellae between the pillars are nanogranular (Fig. 7J), granules being embedded in an abundant matrix, probably organic as shown by AFM phase image (Fig. 7K, L). It must be noted that in adult shell, pillars merged in a zig zag pattern, while they are clearly separated and curly in embryonic shells (Fig. S2G).

Incubation of embryos in calcein-containing seawater reveals that calcification occurs in the pillars as soon as they start to grow from a dorsal septum to the future ventral one. The calcification is particularly located at the distal branching ends of each pillar until they connect with a new septum in formation (Fig. S2H, I).

Rostrum

In the adult shell, the rostrum is clearly visible as a sharp curved spine (Fig. 8A, B). Such sections also show the topographic relationships between the ventral fold, the fork, the dorsal shield and the first septa (Fig. 8A-C). The concentric structure is displayed in a transverse fracture (Fig. 8D) whereas the layered arrangement is shown in longitudinal sections (Fig. 8E, F). Despite the continuity between the dorsal shield and the rostrum, the growth layers of the rostrum are thinner and more regular than those of the dorsal shield (Fig. 8F), the rostrum being smaller and smoother than the dorsal surface of the shell. No tubercle is present on the rostrum. The thickness of the growth layers is variable, and these layers are composed of parallel elongated crystallites, similar to those of the dorsal shield (Fig. 8G). Depending on the orientation of the section and the thickness of the growth layers, the crystallites are more or less visible.

The rostrum is not developed at the studied embryonic stages (Fig. 1D-F, Fig. 8H-I). It starts to differentiate from one month, after hatching.

Fork - ventral process

Fork is in contact and inserted on the inner prismatic layer of the dorsal shield (Fig. 8C, 9A). The fork is composed of parallel lamellae, the thickness of which is similar to those of the septa (Fig. 9B). Depending on the orientation of the fracture, the aspect of the lamellae differs (Fig. 9B, C), but a closer examination shows that the compact lamellae comprise two sublayers: one sublayer is “prismatic” (Fig. 9D, 1), the second one being more “lamellar” (Fig. 9D: 2). The boundary between these two sublayers is not distinct, and their thickness is irregular. Thus, in some fractures, one of these sublayers is not pulled out (Fig. 9C).

The ventral fold, also called ventral process (Fig. 8A-B), shows a radial structure, composed of a series of thin organic and mineralized layers (Fig. 9E). The prismatic structure of the mineralized layers is similar to that of the outer layer of the dorsal shield (Fig. 9F).

Fork and ventral process are not differentiated in the embryonic shells (Fig. 1C, 4A, E).

Composition of adult and embryonic samples

The spectra of the calcite and aragonite groups are characterized by three major bands attributed to the carbonate ion CO_3^{2-} : ν_3 at 1429 cm^{-1} , the ν_2 doublet $877 - 848\text{ cm}^{-1}$, and ν_4 at 713 cm^{-1} for the calcite group; ν_3 at 1471 cm^{-1} and two doublets: ν_2 at $858 - 844\text{ cm}^{-1}$ and ν_4 at $713 - 700\text{ cm}^{-1}$ for the aragonite group (Adler and Kerr 1963). The weak ν_1 band is at 1012 cm^{-1} for calcite and at 1083 cm^{-1} for aragonite (Jones and Jackson 1993). According to Ylmen and Jäglid (2013), the ν_3 asymmetric stretching of CO_3^{2-} has a larger wavenumber range from 1425 and 1590 cm^{-1} .

The FTIR spectrum of the geological aragonite used as standard shows these main features (Fig. 10).

The dorsal shield and ventral chambered zone of adult shells also displayed the main bands assigned to aragonite: ν_1 at 1083 cm^{-1} , ν_2 doublet at $860\text{-}878\text{ cm}^{-1}$ and a doublet ν_4 at $700\text{-}713\text{ cm}^{-1}$. Strong bands are visible respectively at 1512 and 1514 cm^{-1} . Unfortunately, in this region ($1400\text{-}1600\text{ cm}^{-1}$), protein and chitin have characteristic amide I and II bands, and aragonite has an intense ν_3 vibration band at 1483 cm^{-1} . The spectral pattern between 1644 and 1510 cm^{-1} shows 2 intense bands probably indicative of a mixture of organic and mineral (CO_3^{2-}) components. The bands at 1657 and 1644 cm^{-1} could be attributed to amide I vibration, whereas, the bands at 1512 and 1514 cm^{-1} are probably a mixture of amide II and $\nu_3\text{ CO}_3^{2-}$ vibrations.

1
2
3
4 Sugars are common components of the organic matrices extracted from mollusc shells. Bands
5 between 1050 and 1150 cm^{-1} are known to be characteristic for sugars. Although these bands are
6 not clearly observed on both spectra, previous results (Le Pabic et al. 2017) and Fig S3 confirm
7 the presence of sugars (large CO vibration band around 1030-1070 cm^{-1}). The main part of the
8 dorsal shield is the prismatic outer layer, low in organic components. Organic matrices in the
9 form of abundant lamellae exist in the ventral part, so that chitin is more abundant.

10
11
12
13
14
15 The size of embryonic samples does not allow to separate the dorsal shield and the septa,
16 so that the whole samples were powdered for FTIR analyses. The “mineral bands” (v1 to v4, Fig.
17 10) are weak. As observed in the adult spectra, 1456 and 1639 cm^{-1} bands can be assigned to
18 amide vibrations from both proteins and chitin. The characteristic sugar band at 1030-1070 cm^{-1}
19 is probably hidden by the spectrum background (as also observed for the adult spectra).

20
21
22
23
24 To sum up, in all non decalcified samples, bands assigned to organic components are
25 present, but they represent a mixture of proteins, chitin and lipids, so that a precise assignment is
26 not possible. Spectra of the embryonic (green) and adult (orange and blue) shells are indicative of
27 a mixed mineral - organic composition, with very low mineral content in the case of the juvenile
28 shell.

29
30
31
32
33 One of the advantages of Raman spectroscopy is the small size of the beam ($\sim 5 \mu\text{m}$ with the
34 green laser), allowing precise *in situ* punctual analyses. Regarding the first appearance of
35 mineralisation, this was detected by micro-Raman spectroscopy at stage 25. The spectrum
36 obtained (Fig. 11) is characteristic of a crystalline polymorph of calcium carbonate, more
37 precisely aragonite, with main peaks at 152, 206, 701-705 and 1085 cm^{-1} (Urmos et al. 1991;
38 Wehrmeister et al. 2011). The strongest band at 1085 cm^{-1} is an internal mode that derives from
39 the symmetric stretching mode (v1) of carbonate ions. The peaks visible at 152 and 206 cm^{-1}
40 correspond to translational and rotational lattice modes of aragonite carbonate ions, respectively.
41 The doublet 701- 705 cm^{-1} , specific for aragonite, corresponds to the in-plane bending (v4) mode
42 of aragonite carbonate ions.

43
44
45
46
47
48 Moreover, aragonite is already present whatever the parts of the cuttlebone analysed
49 (pillar, septa, even at the level of the chamber in formation), suggesting that the calcification is
50 concomitant to the growth process. Note that ACC (amorphous calcium carbonate, precursor of
51 any crystalline polymorph) was never evidenced. The mineralization seems to be happening
52 directly as aragonite.

Discussion

Anatomy and structure

The anatomy and organisation of the adult cuttlebone of *Sepia* are known since the work of Appellöf (1893). Since, the relationships between the different elements (rostrum, fork...) have been more precisely defined (Dauphin 1979, 1981; Cadež et al. 2017).

In *Sepia officinalis*, the septa as well as the dorsal shield are made of three layers, a thick “prismatic” outer layer, a lamello-fibrillar “nacre” and a thin “prismatic” inner layer. All layers are built with elongated acicular crystallites, parallel to the surface of the shell in the lamello-fibrillar “nacre”, perpendicular in the prismatic layers. These last ones, from a morphological point of view and despite they are called “prismatic”, clearly differ from other aragonitic prismatic layers known in other mollusc shells (e.g., Unionids: Dauphin et al. 2017, Schoeppler et al. 2018). The crystallites are not organized in large prisms, the reason why these layers are called “fibres” in some taxa. These prismatic layers are more similar to the aragonitic “fibres” from coral skeletons (Cuif and Dauphin 2005; Cuif 2016). The absence of tablets in the lamello-fibrillar “nacre” is also confirmed.

The lamellar aspect observed for all the layers and the presence of parallel elongated crystallites were described by Grégoire (1961), then Mutvei (1964). The changes in the crystallite orientation at every lamella as well as the absence of tablets were also observed by these authors. Since, SEM observations have confirmed that such a structure is present in *Spirula* (Dauphin 1976; Bandel and von Boletzky 1979), and belemnites (Doguzhaeva et al. 2003).

All the modern cephalopod shells are aragonitic, with different structures. The prismatic layers are diverse in structure and thickness. For example, in modern shells, the lamellar layer is thick and calcified (as here in *Sepia* but also in *Nautilus*) or very thin and organic (outer wall in *Spirula*). Note that in *Spirula*, the nacreous layer is the thickest part of the septa and is strongly mineralized (Mutvei 1964).

The outer surface of the dorsal shield of *Sepia* is not smooth, and the presence of tubercles is due to irregular spherulites. In the outer layer of the shell of *Nautilus*, irregular spherulites also exist, so that this layer is said to be spherulitic prismatic (Mutvei 1964). Similar

1
2
3
4 structures also exist in fossil genera: *Belosepia*, *Beloptera* and *Belopterina* (Dauphin, 1984,
5
6 1985, 1986).

7
8 Despite these different microstructures, high-resolution SEM and especially AFM reveal,
9
10 at the nanolevel, that all the aragonitic layers are made of rounded heterogeneous granules
11
12 (diameter < 100 nm). The abundance of the organic matrices, around (and probably within) the
13
14 granules, is shown by AFM phase images and BSE-SEM images.

15
16 Another feature is the complex structure of the pillars. Not only they show an organic
17
18 envelope, growth zones and granules, but transversal sections reveal that their inner structure is
19
20 heterogeneous: the central zone is sometimes empty or is more organic than the outer layer. (Fig.
21
22 S2C, D). It must be added that the shape of the pillars is not constant: curly and isolated in the
23
24 embryo, they are connected in zig zag wall in the adult shell.

25
26 All the morphological elements found in the adult shell exist in the embryonic shell but
27
28 only the dorsal shield and the septa with pillars are visible at the hatching phase. The anatomy of
29
30 the first stages of the cuttlebone has been described but most studies are focused on the number
31
32 of septa and shape of the pillars. The cuttlebone of *Sepia officinalis* appears at stage 24 as a fully
33
34 organic structure in a closed shell sac, the first calcified layers appear between stage 24 and 25
35
36 and the first pillars are built as soon as the formation of the second septa with the formation of
37
38 the first chamber (Bandel and Boletzky 1979, Le Pabic et al. 2016).

39
40 The three layers of the dorsal shield are visible, despite the microstructural elements
41
42 (prisms or lamello-fibrillar nacre) are not so well differentiated. Embryonic shell shows that
43
44 growth lines are visible in the pillars of the ventral part as soon as stage 29 (Le Pabic et al. 2016).
45
46 They are also clearly visible in SEM images, as well as the prismatic structure. Rostrum is a
47
48 weak bump at stage 30, with a structure similar to that of the dorsal shield. Fork and ventral
49
50 process are not differentiated in the newly hatched shell, and “wings” are absent or not
51
52 developed. They are lateral extensions of the dorsal shield (Barskov 1973; Dauphin 1981), and
53
54 their surface is granular (Fig. S2F).

55
56 In most fossil sepiids, the ventral region and the fragile structure of the pillars are not
57
58 preserved. Lamellae and pillars are visible in Miocene Sepiids from Australia, but their inner
59
60 structure is not displayed (Košťák et al. 2017). A change in wall/pillar configuration between the
61
62 different regions of the cuttlebone (lateral areas vs median and latero-median areas) has been
63
64 reported both in *Sepia* (extant species) and *Belosaepia* (fossil species) (Sherrard 2000; Yancey et
65

1
2
3
4 al. 2010). A recent study performed using CT-scan study did not evidenced such a difference in
5
6 adult *Sepia* cuttlebone (Le Pabic et al. 2019). Actually Košťák et al. (2016) have not evidenced
7
8 any imprints of pillar in the exceptionally preserved embryonic part of the holotype of *S.*
9
10 *vindobonensis*, or in specimen NHMW 2004z0076/0039 of *S. aff. sanctacrucensis*. In this case,
11
12 the development of pillars in the embryonic shell of extant cephalopods could represent an
13
14 evolutionary novelty. Nevertheless, our results have shown that calcification of the embryonic
15
16 shell is very light so that it cannot be excluded that these very small embryonic pillars have
17
18 disappeared during fossilisation.
19

20 21 **Composition**

22 FTIR analyses show clearly that both the embryonic and the adult *Sepia* cuttlebones are
23
24 composed of biogenic aragonite (result confirmed by Raman spectroscopy), which means they
25
26 are made of a mixture of a crystalline polymorph of CaCO_3 and an inner organic matrix. The
27
28 spectra obtained from the powdered dorsal shield and the ventral chambered part exhibit bands
29
30 corresponding mainly to aragonite, proteins, chitin and other carbohydrates. FTIR spectra of the
31
32 soluble and insoluble matrices resulting from the decalcification of the ventral zone and dorsal
33
34 shield have been provided by Le Pabic et al. (2017). Whereas bands associated with proteins
35
36 (vibrational amide bands) appear in the two spectra, bands associated with carbohydrates are
37
38 more important in the insoluble matrix (but stronger in the chambered part than in the dorsal
39
40 shield probably linked to the presence of an abundant matrix inside the chambers).
41

42 43 **Mineralization**

44 Raman analyses allowed deciphering the calcification process during the development of the
45
46 cuttlebone from the embryo to the adult. Until stage 24 embryo, the shell in formation appears
47
48 fully organic. From stage 25, calcification is detected by the presence of bands characteristic of
49
50 CaCO_3 , wherever the area analysed, which means that this process starts in all the cuttlebone at
51
52 the same time. From this stage, the cuttlebone can then be considered as a biomineral, mixture of
53
54 mineral and organic components.

55 Raman and FTIR spectroscopy techniques confirm that the CaCO_3 polymorph of the
56
57 adult is aragonite as already reported. As for this adult shell, although the polymorph is
58
59 crystalline for all the layers, the nanostructure reveals that they are composed of irregular
60
61
62
63
64
65

1
2
3
4 rounded granules as observed for other biogenic crystalline CaCO_3 polymorph (Cuif and
5 Dauphin 2005; Cuif et al. 2012). The maximal observed diameter of the granules is about 100
6 nm. They are not homogenous from a compositional point of view, as shown by AFM phase
7 images, and they are surrounded by a cortex, probably a mixture of organic matrix and
8 amorphous CaCO_3 (although this polymorph was not detected by Raman or FTIR methods).
9

10
11 In embryos, despite the transparency and fragility of the shell structures, using Raman
12 spectroscopy we demonstrate for the first time that a light mineralization appears at stage 25
13 directly as aragonite. Mineralization remains light until hatching, occurring from this stage
14 concomitantly to the growth of the shell. For example, the calcein-labelling method evidenced
15 that the growth and calcification of the pillars occur simultaneously from a new septum towards
16 the branched distal ends of these pillars.
17

18
19 Inside the egg, the embryo feeds only with maternal yolk and the perivitelline fluid
20 surrounding the embryo has more or less the same composition than the seawater, with ions
21 passing through the envelope. But as the embryo is in a protected environment, the shell has not
22 a real function. The main source of calcium comes from food after hatching and the position in
23 the water column changes, leading to an environmental medium richer in calcium. As a
24 consequence, the developing shell becomes hardly mineralized. The Raman spectra show that
25 there is no modification of the mineral type between the embryonic shell inside the egg and the
26 adult shell: mineral is aragonite as soon as it could be detected in embryo. It is not excluded that
27 mineralization could start earlier as ACC (amorphous calcium carbonate) but this was not
28 detected.
29
30
31
32
33
34
35
36
37
38
39
40
41
42
43
44
45

46 **Conclusion**

47
48 The examination of adult shells of *Sepia officinalis* shows that despite a particular morphology,
49 the main layers of the cephalopod shell are present. The dorsal shield comprises three layers, the
50 thickness and mineralization degree of which differs. The ventral part (pillars and lamellae)
51 represents the septa and the siphuncular zone.
52

53
54 In both septa and dorsal shield, the middle layer is lamellar, with acicular crystallites, as
55 the classical nacreous layer but the tablets are absent. Pillars of the ventral zone are not
56
57
58
59
60
61
62
63
64
65

homogeneous: the inner part is more organic than the outer part, as displayed by longitudinal and transverse sections. Rostrum, absent in embryo, is an extension of the dorsal shield.

Despite differences in the structure of the layers, and despite the crystalline structure of the constitutive mineral, all microstructural units are composed of more or less rounded granules (diameter between 50 and 100 nm). The organic matrix contains mainly chitin and proteins, but also, in a lesser extent, other carbohydrates and lipids, as in all the calcified biominerals.

In the embryonic shell, an early mineralization, directly as aragonite, is detected at stage 25. At stages 28 and 29, before hatching, the shell has about 6 chambers septa, and is still weakly mineralized. The micro- and nanostructures of the pillars and lamellae of the ventral zone are similar to those of adult shells, despite the pillars are branching, and not yet linked to form undulating walls. Growth lines are visible, as well as granules. Fork, ventral process and rostrum are not yet differentiated. Chitin is probably the main component of the embryonic shell, and FTIR profile is more similar to the ventral zone of an adult shell (less mineralized) than to the dorsal shield.

Acknowledgements

This work was financially supported by the ATM "Interactions Minéral - Vivant" funding of the Muséum national d'Histoire naturelle (SEPIOM project). The authors thank all the members of the Max Planck Institute for Interfaces and Colloids (Golm, Germany) for their help. We thank C. Jozet-Alves and the CREC (University of Caen) for providing eggs of *Sepia officinalis*. LBP thanks G. Patriache and L. Largeau (CNRS-LPN) for the first tests on mineral composition of embryonic shell several years ago.

Compliance with ethical standards

Animal protocols were carried out in accordance with European legislation (directive 2010-63-UE and French decree 2013-118).

Conflict of interest

Authors declare that they have no conflict of interest.

Research involving human and animal participants

We neither used endangered species nor were the investigated animals collected in protected areas.

References

- Adler HH, Kerr PF (1963) Infrared absorption frequency trends for anhydrous normal carbonates. *Am Mineral* 48:839-853
- Allcock AL, Lindgren A, Strugnell J (2015) The contribution of molecular data to our understanding of cephalopod evolution and systematics: a review. *J Nat History* 49:1373-1421
- Appellöf A (1893) Die Schalen von *Sepia*, *Spirula* und *Nautilus*. Studien über den Bau und das Wachstum. *K Svenska Akad Handl Stockholm* 25(7):1-106
- Bandel K (1990) Cephalopod shell structure and general mechanisms of shell formation. In: *Skeletal Biomineralization: Patterns Processes and Evolutionary Trends*, Vol 1, Carter JG (ed). Van Nostrand Reinolds, New York, pp 97-115
- Bandel K, Boletzky S von (1979) A comparative study of the structure, development and morphological relationships of chambered cephalopod shells. *Veliger* 21(3):313-354
- Barskov IS (1973) Microstructure of the skeletal layers of *Sepia* and *Spirula* compared with the shell layers of other molluscs. *Paleont J* 3:285-294
- Bettencourt V, Guerra A (2001) Age studies on daily growth increments in statoliths and growth lamellae in cuttlebone of cultured *Sepia officinalis*. *Mar Biol* 139:327-334
- Boggild OB (1930) The shell structure of the molluscs. *D Kgl Danske Vidensk Selsk Skr, naturvidensk og mathem* 9(2):231-326
- Boletzky S von, Andouche A, Bonnaud-Ponticelli L (2016) A developmental table of embryogenesis in *Sepia officinalis*. *Vie Milieu* 66(1):25-34
- Butler-Struben HM, Brophy SM, Johnson MA, Crook RJ (2018) In vivo recording of neural and behavioral correlates of anesthesia induction, reversal, and euthanasia in cephalopod molluscs. *Front Physiol* 9:109. doi: 10.3389/fphys.2018.00109

- Cadež V, Škapin SD, Leonardi A, Križaj I, Kazazic S, Salopek-Sondi B, Sondi I (2017) Formation and morphogenesis of a cuttlebone's aragonite biomineral structures for the common cuttlefish (*Sepia officinalis*) on the nanoscale: Revisited. J Colloid Interface Sci 508:95-104
- Checa AG, Cartwright JHE, Sanchez-Almazo I, Andrade JP, Ruiz-Raya F (2015) The cuttlefish *Sepia officinalis* (Sepiidae, Cephalopoda) constructs cuttlebone from a liquid-crystal precursor. Sci Rep 5:11513. doi: 10.1038/srep11513
- Cuif JP (2016) Calcification in the Cnidaria through time: an overview of their skeletal patterns from individual to evolutionary viewpoints. In: The Cnidaria, Past, Present and Future, Goffredo S, Dubinsky Z (eds) Springer, pp 163-179
- Cuif JP, Dauphin Y (2005) The two-step mode of growth in the scleractinian coral skeletons from the micrometre to the overall scale. J Struct Biol 150:319-331
- Cuif J, Dauphin Y, Denis A, Gaspard D, Keller JP (1983) Etude des caractéristiques de la phase minérale dans les structures prismatiques du test de quelques Mollusques. Bull Mus Natl Hist Nat, Paris, 4è sér, 5 A, 3:679-717
- Cuif JP, Bendounan A, Dauphin Y, Nouet J, Sirotti F (2013) Synchrotron-based photoelectron spectroscopy provides evidence for a molecular bond between calcium and mineralizing organic phases in invertebrate calcareous skeletons. Anal Bioanal Chem 405(27): 8739-8748
- Dauphin Y (1976) Microstructure des coquilles de Céphalopodes: I. *Spirula spirula* L. (Dibranchiata, Decapoda). Bull Mus natn hist nat, Paris, 3è sér., 382, Sciences de la terre 54: 197-238.
- Dauphin Y (1979) Organisation ultrastructurale de l'os de seiche (Cephalopoda-Dibranchiata) C R Acad Sc Paris D 288: 619-622
- Dauphin Y (1981) Microstructures des coquilles de Céphalopodes. II- La seiche (Dibranchiata, Decapoda). Palaeontogr A176:35-51
- Dauphin Y (1984) Microstructures des coquilles de Céphalopodes. IV- Le "rostre" de *Belosepia* (Dibranchiata). Palaeontogr Z 58(1/2):99-117
- Dauphin Y (1985) Microstructural studies on cephalopod shells. V- the apical part of *Beloptera* (Dibranchiata, Tertiary). N Jb Geol Palaeont Abh 170(3):323-341

- Dauphin Y (1986) Microstructure des coquilles de Céphalopodes: la partie apicale de *Belopterina* (Coleoidea). Bull Mus natn Hist nat, Paris, 4e sér., 8, section C 1: 53-75
- Dauphin Y, Keller JP (1982) Mise en évidence d'un type microstructural coquillier spécifique des Céphalopodes dibranchiaux. C R Acad Sc Paris sér. II 294:409-412
- Dauphin Y, Luquet G, Salomé M, Bellot-Gurley L, Cuif JP (2017) Structure and composition of *Unio pictorum* shell: arguments for the diversity of the nacroprismatic arrangement in molluscs. J Microscopy 270(2):156-169
- Dauphin Y, Williams CT, Barskov IS (2007) Aragonitic rostra of the Turonian belemnite *Goniocamax*: Arguments from diagenesis. Acta Palaeont Pol 52:85-97
- Degens ET, Spencer DW, Parker RH (1967) Paleobiochemistry of molluscan shell proteins. Comp Biochem Physiol 20(2):553-579
- Doguzhaeva L, Dunca E (2015) Siphonal zone structure in the cuttlebone of *Sepia officinalis*. Swiss J Palaeontol 134:167-176
- Doguzhaeva L, Mutvei H, Weitschat W (2003) The pro-ostracum and primordial rostrum at early ontogeny of lower Jurassic belemnites from North-Western Germany. In: Coleoid cephalopods through time, Warnke K, Keupp H, Boletzky von S (eds) Berliner Paläobiol Abh 03, pp 79-89
- Dorey N, Melzner F, Martin S, Oberhänsli F, Teyssié JL, Bustamante P, Gattuso JP, Lacoue-Labarthe T (2013) Ocean acidification and temperature rise: effects on calcification during early development of the cuttlefish *Sepia officinalis*. Mar Biol 160:2007-2022
- Drozdova TV, Karyakin AV, Krasnova VA (1971) Chemical composition and infra-red absorption spectra of the organic matrix of the shell in the squid *Sepia pharaonis*. J Evol Biochem Physiol 7(4):350-356
- Ehrenberg C.G. (1828-1831). Animalia evertebrata exclusis Insectis. Series prima. In: F.G. Hemprich & C.G. Ehrenberg, Symbolae physicae, seu icones et descriptiones Mammalium, Avium, Insectorum et animalia evertebra, quae ex itinere per Africam borealem et Asiam occidentalem studio nova aut illustrata redierunt. 126 pp. (1831), 10 pls (1828)
- Erben (1972) Über die Bildung und das Wachstum von Perlmutter. Biomineralisation 4:15-46.

- Florek M, Fornal E, Gomez-Romero P, Zieba E, Paszkowicz W, Lekki J, Nowak J, Kuczumow A (2009) Complementary microstructural and chemical analyses of *Sepia officinalis* endoskeleton. *Mater Sci Engin C* 29:1220-1226
- Grégoire C (1961) Sur la structure de la nacre septale des Spirulidae, étudiée au microscope électronique. *Arch Int Physiol Biochim* 69(3):374-377
- Grégoire C (1967) Sur la structure des matrices organiques des coquilles de mollusques. *Biol Rev* 42:653-688
- Gutowska MA, Pörtner HO, Melzner F (2008) Growth and calcification in the cephalopod *Sepia officinalis* under elevated seawater pCO₂. *Mar Ecol prog Ser* 373:303-309
- Haas W (2003) Trends in the evolution of the Decabrachia. *Berliner Paläobiol Abh* 3:11-12
- Hunt S, Nixon M (1981) A comparative study of protein composition in the chitin-protein complexes of the beak, pen, sucker disc, radula and oesophageal cuticle of cephalopods. *Comp Biochem Physiol* 68B:535-546
- Jones GC, Jackson B (1993) Infrared transmission spectra of carbonate minerals. Springer Science, 239 pp
- Karthika R, Manigandan V, Saravanan R, Rajesh RP, Chandrikada B (2016) Structural characterization and *in vitro* biomedical activities of sulfated chitosan from *Sepia pharaonis*. *Int J Biol Macromol* 84:319-328
- Kim BS, Kim JS, Sung HM, You HK, Lee J (2012) Cellular attachment and osteoblast differentiation of mesenchymal stem cells on natural cuttlefish bone. *J Biomed Mater Res* 100A:1673-1679
- Košťák M, Schlögl J, Hudácková N, Kroh A, Halásová E, Gašparič R, Matúš Hyžný, Wanzenböck G (2016) *Sepia* from the Miocene of the Central Paratethys: new taxa and notes on late Cenozoic cuttlefish diversity. *J System Paleontol* 14(12):1033-1057
- Košťák M, Ruman A, Schlögl J, Hudácková N, Fuchs D, Mazuch M (2017) Miocene sepiids (Cephalopoda, Coleoidea) from Australia. *Foss Rec* 20:159-172
- Kröger B, Vinther J, Fuchs F (2011) Cephalopod origin and evolution: A congruent picture emerging from fossils, development and molecules. *Bioessays* 33:602-613
- Le Pabic C, Rousseau M, Bonnaud-Ponticelli L, Boletzky S von (2016) Overview of the shell development of the common cuttlefish *Sepia officinalis* during early-life stages. *Vie et Milieu* 66(1):35-42

- 1
2
3
4 Le Pabic C, Marie A, Marie B, Percot A, Bonnaud-Ponticelli L, Lopez PJ, Luquet G (2017) First
5
6 proteomic analyses of the dorsal and ventral parts of the *Sepia officinalis* cuttlebone. J
7
8 Proteomics 150:63-73
9
- 10 Le Pabic C, Derr J, Luquet G, Lopez P-J, Bonnaud-Ponticelli L (2019) Three-dimensional
11
12 structural evolution of the cuttlefish *Sepia officinalis* shell from embryo to adult stages. J
13
14 R Soc Interface 16(158): 20190175. doi: 10.1098/rsif.2019.0175
- 15 Lemaire J (1970) Table de développement embryonnaire de *Sepia officinalis* L. (Mollusque,
16
17 Céphalopode). Bull Soc zool Fr 95:773-782
18
- 19 Linnaeus C. (1758). Systema Naturae per regna tria naturae, secundum classes, ordines, genera,
20
21 species, cum characteribus, differentiis, synonymis, locis. Editio decima, reformat [10th
22
23 revised edition], vol. 1: 824 pp.
- 24 Lowenstam HA, Weiner S (1989) On Biomineralization, Oxford University Press, 323 pp
25
- 26 Marie B, Marin F, Marie A, Bédouet L, Dubost L, Alcaraz G, Milet C, Luquet G (2009)
27
28 Evolution of nacre: biochemistry and proteomics of the shell organic matrix of the
29
30 cephalopod *Nautilus macromphalus*, Eur J Chem Biol 10:1495-1506
31
- 32 Mutvei H (1964) On the shells of *Nautilus* and *Spirula* with notes on the shell secretion in non
33
34 cephalopod mollusks. Arkiv Zool 16:221-278
- 35 Mutvei H (1970) Ultrastructure of the mineral and organic components of molluscan nacreous
36
37 layers. Biomineralisation 2:48-61
38
- 39 Mutvei H (2016) Siphuncular structure in the extant *Spirula* and other Coleoids (Cephalopoda).
40
41 GFF 139(2):129-139
42
- 43 Naef A (1922) Die fossilen Tintenfische. Carl Fisher ed., Jena, 322 pp
44
- 45 Naef A (1928a) Die Cephalopoden Embryologie. In Fauna und Flora des Golfes von Neapel und
46
47 der angrenzenden Meeres- Abschnitte. Berlin, Friedländer, 357 pp
- 48 Naef A (1928b) Die Cephalopoden. In: Fauna und Flora des Golfes von Neapel. Verlag, von R.
49
50 Friedländer & Sohn, Berlin, 863 pp
51
- 52 Ogasawara W, Shenton W, Davis SA, Mann S (2000) Template mineralization of ordered
53
54 macroporous chitin-silica composites using a cuttlebone-derived organic matrix. Chem
55
56 Mater 12:2835-2837
- 57 Schoeppler V, Granasy L, Reich E, Poulsen N, de Kloe R, Cook P, Rack A, Pusztai T, Zlotnikov
58
59 I (2018) Biomineralization as a paradigm of directional solidification: A physical model
60
61
62
63
64
65

- for Molluscan shell ultrastructural morphogenesis. *Adv Mater* 30(45): e1803855. doi: 10.1002/adma.201803855
- Sen H (2013) The cuttlebone development of common cuttlefish [*Sepia officinalis* (Linneaus, 1758)]. *Ege J Fish Aqua Sci* 30:105-108
- Sherrard KM (2000) Cuttlebone morphology limits habitat depth in eleven species of *Sepia* (Cephalopoda: Sepiidae). *Biol Bull* 198:404-414
- Sigwart JD, Lyons G, Fink A, Gutowska MA, Murray D, Melzner F, Houghton JDR, Hu MY (2015) Elevated pCO₂ drives lower growth and yet increased calcification in the early life history of the cuttlefish *Sepia officinalis* (Mollusca: Cephalopoda). *ICES J Mar Sci* 73:970-980
- Sykes AV, Domingues P, Andrade JP (2014) *Sepia officinalis*. In: Iglesias J, Fuentes L, Villanueva R (eds), *Cephalopod Culture*. Springer, Dordrecht, pp 175-204
- Urmos, J., Sharma, S.K., Mackenzie, F.T. (1991) Characterization of some biogenic carbonates with Raman spectroscopy. *Am Mineral* 76:641-646
- Wehrmeister U, Jacob DE, Soldati AL, Loges N, Häger T, Hofmeister W (2011) Amorphous, nanocrystalline and crystalline calcium carbonates in biological materials. *J Raman Spectrosc* 42:926-935
- Winlow W, Polese G, Moghadam H-F, Ahmed IA, Di Cosmo A (2018) Sense and Insensibility - An appraisal of the effects of clinical anesthetics on Gastropod and Cephalopod molluscs as a Step to Improve welfare of Cephalopods. *Front Physiol* 9:1147. doi: 10.3389/fphys.2018.01147
- Yancey TE, Garvie CL, Wicksten M (2010). The middle Eocene *Belosaepia ungula* (Cephalopoda: Coleoidea) from Texas: structure, ontogeny and function. *J Paleontol* 84(2):267-287
- Ylmen R, Jäglid U (2013) Carbonation of Portland cement studied by diffuse reflection Fourier transform infrared spectroscopy. *Int J Concr Struct Mater* 7(1):119-125

Legends of figures

Fig. 1 Comparison of the morphologies of adult and embryonic shells of *Sepia officinalis*.

A-B Views of an adult shell showing the main morphological parts, **A** Ventral view, **B** Dorsal view. **C** Dorsal view of a stage 29 embryonic shell. **D-F** *In situ* localisation of embryonic shells, **D** Lateral view on a stage 27 embryo (X-ray image, note the mineralized statocysts anteriorly - st), **E** Dorsal view on a stage 27 embryo, **F** Dorsal view on a stage 29 embryo. All the shells are shown in the same position, at the top: anterior part, on the bottom: posterior part. (**A-C** photographs, **E-F** optical images, **D** X-ray image)

Fig. 2 Micro- and nanostructure of the outer spherulitic prismatic layer of the dorsal shield of the adult shell of *Sepia officinalis*.

A Oblique fracture showing the outer surface of the dorsal shield with strong tubercles (SE-SEM). **B** Transversal section showing the three layers (BSE-SEM). **C** Detail of the outer spherulitic prismatic layer showing the irregular thickness of the growth layers, and their inner structure composed of acicular crystallites (BSE-SEM). **D** Detail of the elongated crystallites in a growth layer of the outer spherulitic prismatic layer (BSE-SEM). **E** AFM height image of acicular crystallites of the outer spherulitic prismatic layer. **F** AFM phase image showing that acicular crystallites of a polished and etched section comprises rounded granules. **G** AFM phase image of the surface of a growth layer, showing the rounded granules scattered in a dark matrix, probably organic. **H** AFM height image showing a granule in the same sample. **I** AFM phase image of the same zone showing that despite the bleaching, the organic matrix (dark zone) is still abundant so that the outline of the granules is blurred (dotted line). **B-F** Sections polished and etched by formic acid 10% for 2 sec. **G-I** Sections treated by commercial NaOCl (2.6% Cl) for 100 min.

Fig. 3 Micro- and nanostructure of the lamello-fibrillar nacre (A-F) and the inner prismatic layer (G-I) of the dorsal shield of the adult shell.

A Lamello-fibrillar nacre, composed of elongated crystallites parallel to the surface of the layer, with diverse orientations (H₂O₂ 33% for 2 min., 20°C); SE-SEM. **B** Unetched transverse fracture showing the parallel sheets; SE-SEM. **C** Some sheets have substructures (yellow stars); unetched fracture; SE-SEM. **D, E** Two different magnifications of the same zone showing nanogranules

within the sheets ; AFM height image (polished and etched section, acetic acid 2% for 5 sec.). **F** AFM Phase image of the nanogranules showing the abundant organic matrix (D-F same sample). **G** Unetched fracture in the inner prismatic layer showing elongated crystallites; SE-SEM. **H** AFM phase image showing irregular granules (polished and etched section, acetic acid 2% for 5 sec.). **I** Magnification of H showing the heterogeneity of the granules.

Fig. 4 Micro- and nanostructures of the dorsal shield of embryonic shells. **A** stage 24, **B-K** stage 27.

A Organic stage 24 embryonic shell. Septa, wings and rostrum are not differentiated. **B** Longitudinal polished and etched section of a stage 27 embryonic shell showing the dorsal shield and some septa (formic acid 0.1% for 10 sec.). **C** Detail of Fig. 4B showing the insertion of a septum (S) on the dorsal shield (DS); BSE-SEM. **D** Vertical section showing the poorly calcified shell layers. OP: outer spherulitic prismatic layer, IP: inner prismatic layer (section polished and etched by acetic acid 2% for 5 sec.); BSE-SEM. **E** Vertical section showing the irregular thickness of the layers, and the mainly organic middle layer (section polished and etched by formic acid 0.1% for 10 sec.); BSE-SEM. **F** Parallel crystallites in the inner prismatic layer; unetched fracture, BSE-SEM. **G** AFM phase image showing that rounded granules are more or less arranged in columns in some parts of the dorsal shield (section polished and etched by acetic acid 2% for 5 sec.). **H** The size and shapes of the heterogeneous granules are irregular; AFM phase image, same sample. **I** AFM amplitude image showing the rounded granules dispersed in the abundant organic matrix (C: cortex); same sample. **J** AFM phase image of the same area. **K** AFM height image showing the cortex surrounding the granules in a section of the dorsal shield; same sample.

Fig. 5 Morphology of embryonic shell. A-G stage 28, H-J stage 26, K stage 30

A Dorsal view showing the absence of rostrum. **B** Detail of the lateral part of the shell showing growth ridges; dorsal view. **C** Another aspect of the outer surface of the dorsal shield showing two growth rhythms: between the arrows, thin growth layers are visible. **D** First tubercles on the

dorsal surface. **E** Ventral view showing the first septa. **F** Detail of the lateral part showing the first stages of formation of the pillars. **G** Detail of the posterior zone of the ventral surface. (**A-G** SE-SEM pictures). **H-K** After *in vitro* incubation of the embryo in a calcein-containing sea water, the progressive antero-posterior development of the shield covering progressively the growing septum by irregular waves is well visible (**H-I** light microscopy, **J-K** fluorescence microscopy). Note that the development of the pillars in each chamber can be also observed by transparency.

Fig. 6 Micro- and nanostructure of the ventral part of the adult shell.

A Pillar (pi) part of the septa, connected in a zig zag wall inserted on a lamella (L); tangential unetched fracture. **B** Oblique fracture showing the thin lamellae (L) separated by pillars (pi). Pillars are connected by organic membranes (m). **C** Fracture showing the prismatic layer (P) and the lamello-fibrillar nacre (N) of a lamella (L); pillars (pi) are covered by organic membranes (m). **D** Unetched fracture showing growth layers on the surface of a pillar. Insert: the pillar. **E** AFM height image showing growth layers of a pillar (acetic acid 2% for 5 sec.). **F** When the tangential membranes are removed, granules of the pillars are revealed. **G** AFM height image of the rounded granules of a pillar (section polished and etched by acetic acid 0.1% for 5 sec.). **H** Transverse unetched fracture of a pillar (pi) with an enlarged base, the lamello-fibrillar nacreous layer (N) and the prismatic layer (P) of the lamellae (L). **I** Detail showing the parallel crystallites in the lamello-fibrillar nacre. **J** Unetched tangential section of a lamella, showing elongated crystallites in the lamello-fibrillar nacre, the orientation of which differs in the successive sublayers. **K** Unetched oblique section of the lamello-fibrillar nacre, showing the lamellar arrangement; AFM phase image. **L** Unetched surface of the lamello-fibrillar nacre, showing that the variable shapes and orientations of the crystallites. **A, C, L**: SE-SEM images. **B, D-K**: BSE-SEM images.

Fig. 7 Micro- and nanostructure of the ventral zone of the embryonic stage 28 shell.

A Curly aspect of the pillars inserted on a lamella (L) in an unetched tangential fracture; BSE-SEM. **B** Detail of a pillar. **C** Broken pillar showing the enlargement of the basal part, here separated from the lamella; BSE-SEM. **D, E** Surface of a pillar showing the fibrous structure of

the growth layers and the branching towards the insertion on the lamella (L); BSE-SEM. **F** Unetched transverse section of a pillar showing an outer layer and an inner core; BSE-SEM. **G** Section showing the lamello-fibrillar nacre (N) and prismatic (P) layers of a lamella (L) of one of the first septum; BSE-SEM. **H** Similar section, showing the enlargement of the pillar at the insertion on the lamella (L); SE-SEM. **I** Insertion of a septum on the dorsal shield (section polished and etched by acetic acid 2% for 5 sec); BSE-SEM. **J** AFM height image of a polished and etched lamella, showing a granular structure (acetic acid 2% for 5 sec.). **K** AFM phase image showing the abundance of the organic matrix (dark brown); same sample. **L** AFM amplitude image of a granule showing the complex composition of a granule of the lamellae; same sample.

Fig. 8 Rostrum of the adult shell (SE-SEM).

A Polished and etched longitudinal section showing a well-developed rostrum (formic acid 10% for 30 sec.). **B** Section of the posterior part of an adult shell, redrawn from Appellöf (1893). **C** Longitudinal fracture showing the continuity of the outer layer of the dorsal shield and the rostrum. **D** Transverse fracture showing the concentric arrangement of the rostrum. **E** Polished and etched longitudinal section showing the growth layers, and the more or less mineralized zones (formic acid 10% for 30 sec.). **F** Polished and etched longitudinal section showing the axial zone (right part) and the peripheral zone (left part) (H₂O₂ 33% for 13 days, 20°C). **G** Growth layer of the rostrum showing elongated crystallites; unetched sample. **H, I** Dorsal views of the posterior region of embryonic shell (stages 27-30) showing the absence of the rostrum and wings.

Fig. 9 Fork and ventral process, adult shell (SE-SEM)

A Transverse unetched fracture showing the topographic relationships between the dorsal shield, the fork and the ventral part (septa); IP: inner prismatic layer. **B** Detailed view of the contact between the septa and the fork. **C** Unetched fracture showing the lamellar structure of the fork. **D** Detail of the structure of the lamellae of the fork, with a “prismatic” sublayer (1) and a

“lamellar” sublayer (2). **E** Detail of the lamellar structure of the ventral process. **F** Prismatic structure of the mineralized layer of the ventral process.

Fig. 10 Fourier Transform Infrared spectra of a geological aragonite, proteins (BSA), polysaccharides (chitin), embryonic and adult *Sepia* shells.

Fig. 11 Raman spectroscopy analysis of *Sepia* shell showing the presence of aragonite.

A-C Stage 25 embryo. **A** Circular aperture zone corresponding to the first matrix synthesis site. **B** Penultimate chamber (with pillars in formation). **C** Most outer chamber (in formation). **D** adult shell (dorsal shield).

Fig. S1 Terminology used for the orientation of the fractures and polished sections studied using SEM and AFM.

Fig. S2 Variations in morphology and structure of the chambered zone of adult and embryonic shells.

A Enlargement of the basal part of a pillar of an adult shell; fracture fixed and etched (chromium sulphate pH 3.5 for 4 h.); SE - SEM. **B** Pillars are covered by an organic membrane (upper part); under the membrane, the granular structure of the pillar is visible; adult sample. SE - SEM. **C** Etched fracture trough a pillar of an adult shell showing the empty middle part (NaOH 0.5M for 4h at 100°C, pronase pH 7.6 for 6 h at 34°C, chitinase pH 5.6 for 22 h at 24°C); SE - SEM. **D** Etched vertical section through the pillar of an adult shell showing the different behaviour of the middle and external parts (NaOH 1 M for 4h 30 at 100°C, then 4 days at 20°C, lipase 1 mg/ml pH 9 for 28 h at 35°C); SE - SEM. **E** Pillars in the first septa of an adult shell. SE - SEM. **F** Unetched granular surface of the lateral growing edge of a larval shell; BSE - SEM. **G** Unetched tangential fracture showing the zig zag “wall” made by coalescent pillars in an adult shell. **H-I** Stage 25/26 embryonic shell after 24h *in vitro* incubation of the embryo in a calcein-containing sea water (30 mg/L; CNAM, Sigma) followed by 48h incubation in sea water, **H** Optical image,

I Fluorescence image showing that calcification occurs during the growth at the distal extremities of the pillars.

Fig. S3 FTIR spectra of the soluble and insoluble organic matrices extracted from the dorsal shield and ventral zone of an adult shell, showing the similarity between the insoluble matrix and the crab chitin.

The dorsal shield and the ventral zone were mechanically separated in adult samples, immersed in 3% NaClO for 1 h to remove organic contaminants, rinsed with Milli-Q water, dried, and ground into powder by grinding with an electric mortar for 10 min to obtain homogeneous granulometry. Powdered samples were immersed in Milli-Q water and decalcified by progressive addition of 50% acetic acid so that the pH (automatically controlled with a titrimeter) is above 4. The entire extract was centrifuged at 21,000 g for 15 min, which separated the supernatant (soluble) and precipitated (insoluble) fractions. The soluble fraction was desalted by exchange with Milli-Q water on a Microconcentrator (Filtron) using a 3-kDa cut-off membrane and lyophilized. Powdered samples and KBr were oven-dried at 38°C overnight. Then, they were mixed (about 5% powdered samples in KBr) and loaded into the sample cup.

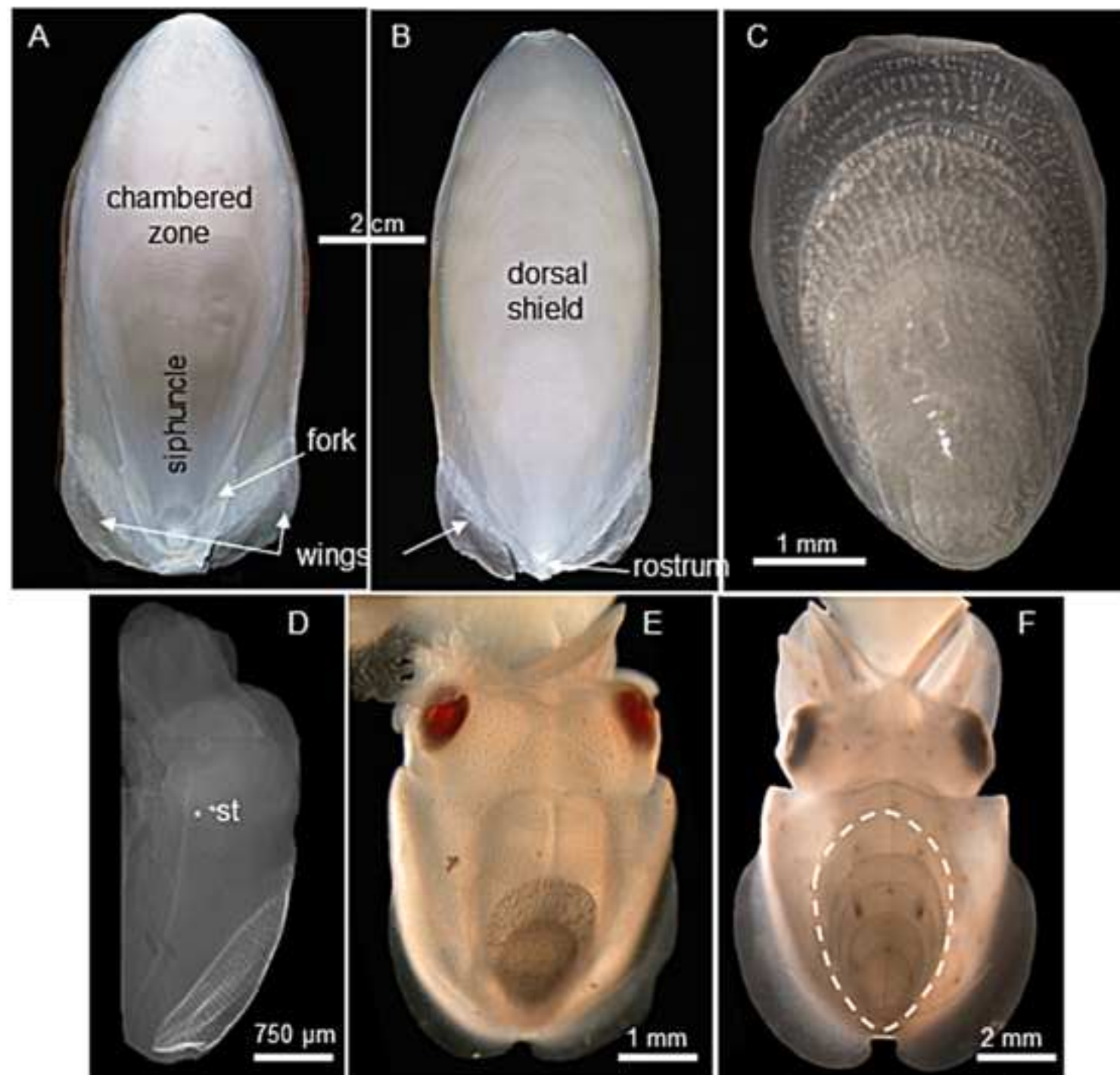


Figure 2

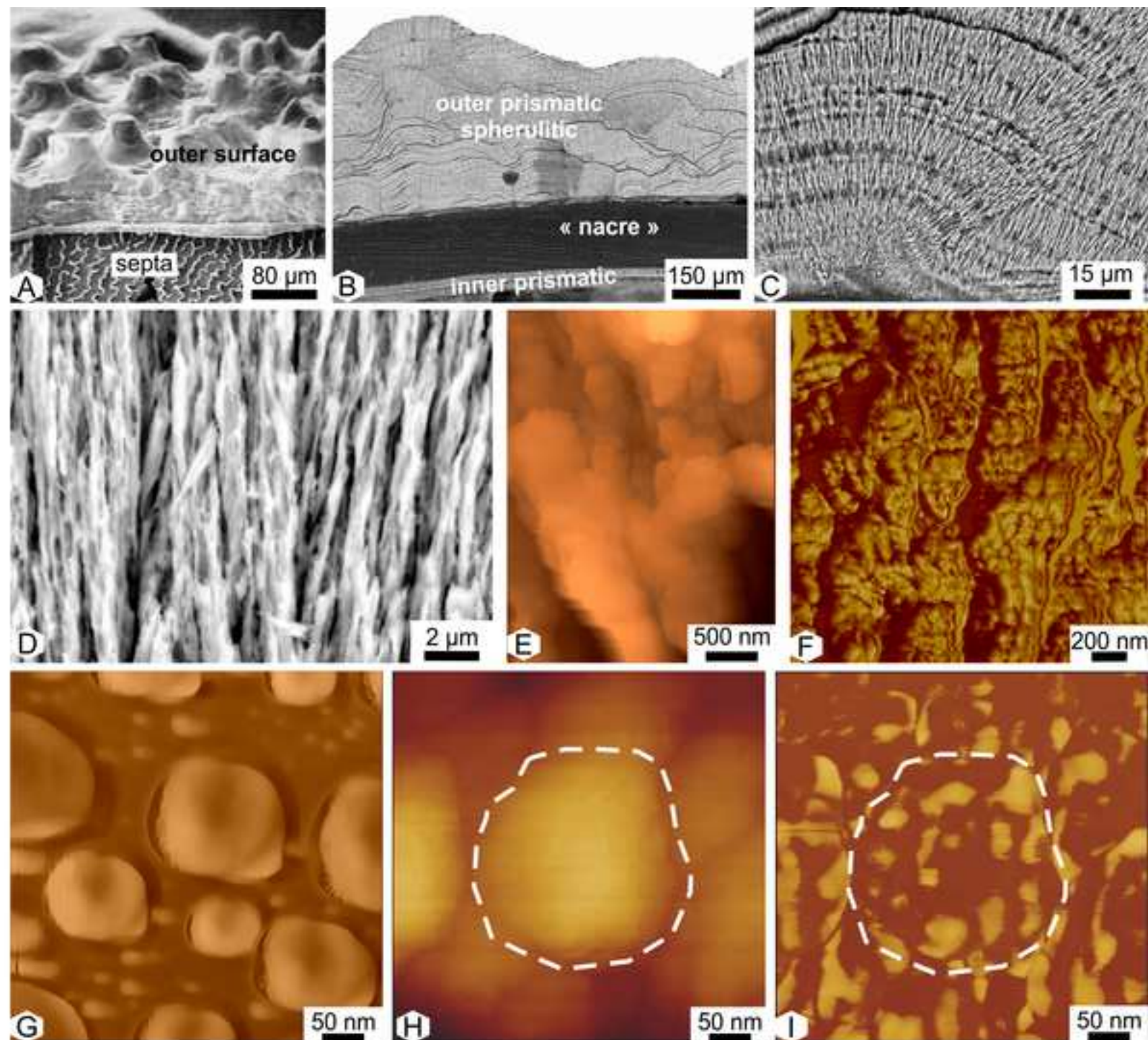


Figure 3

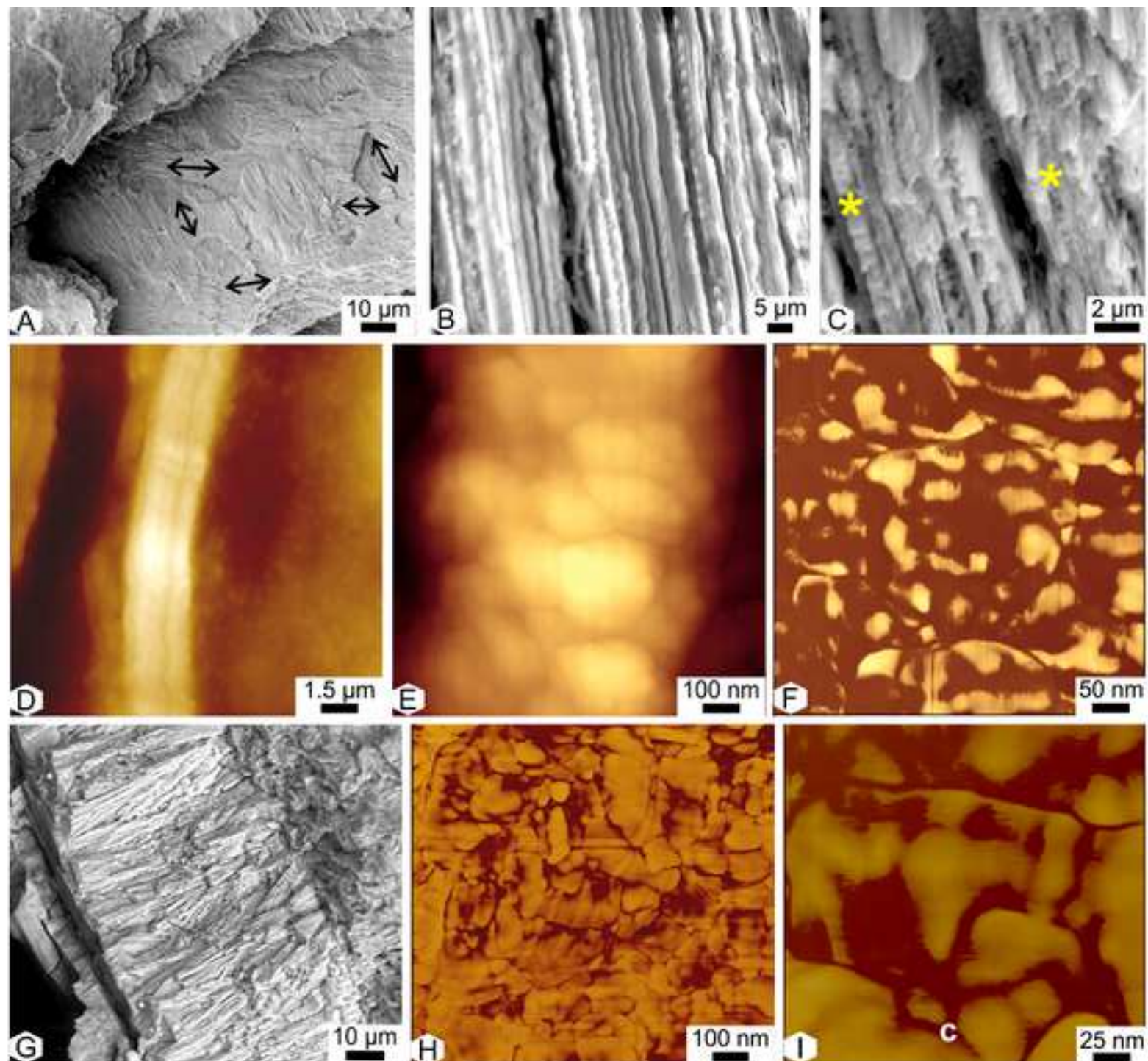
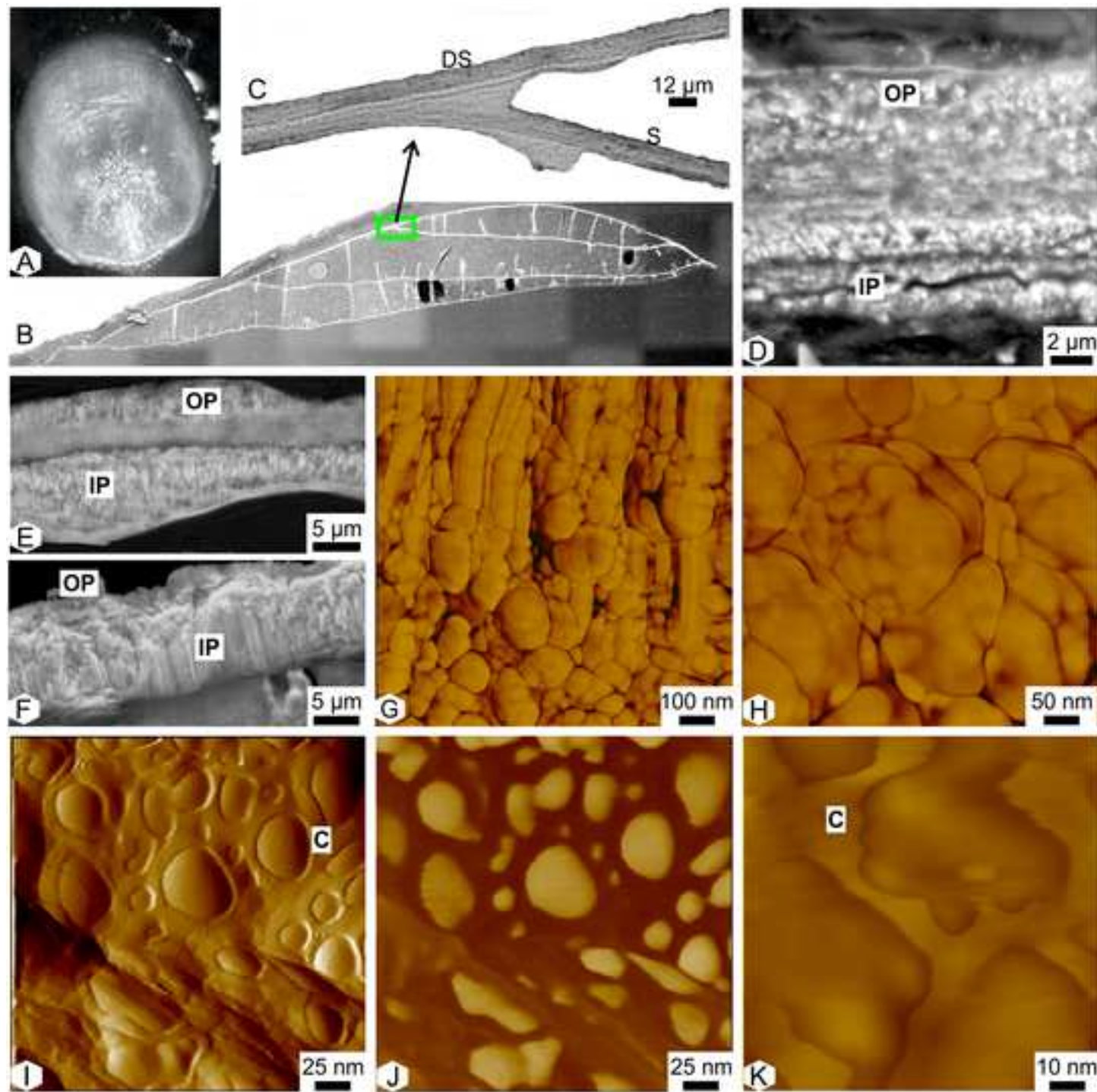


Figure 4



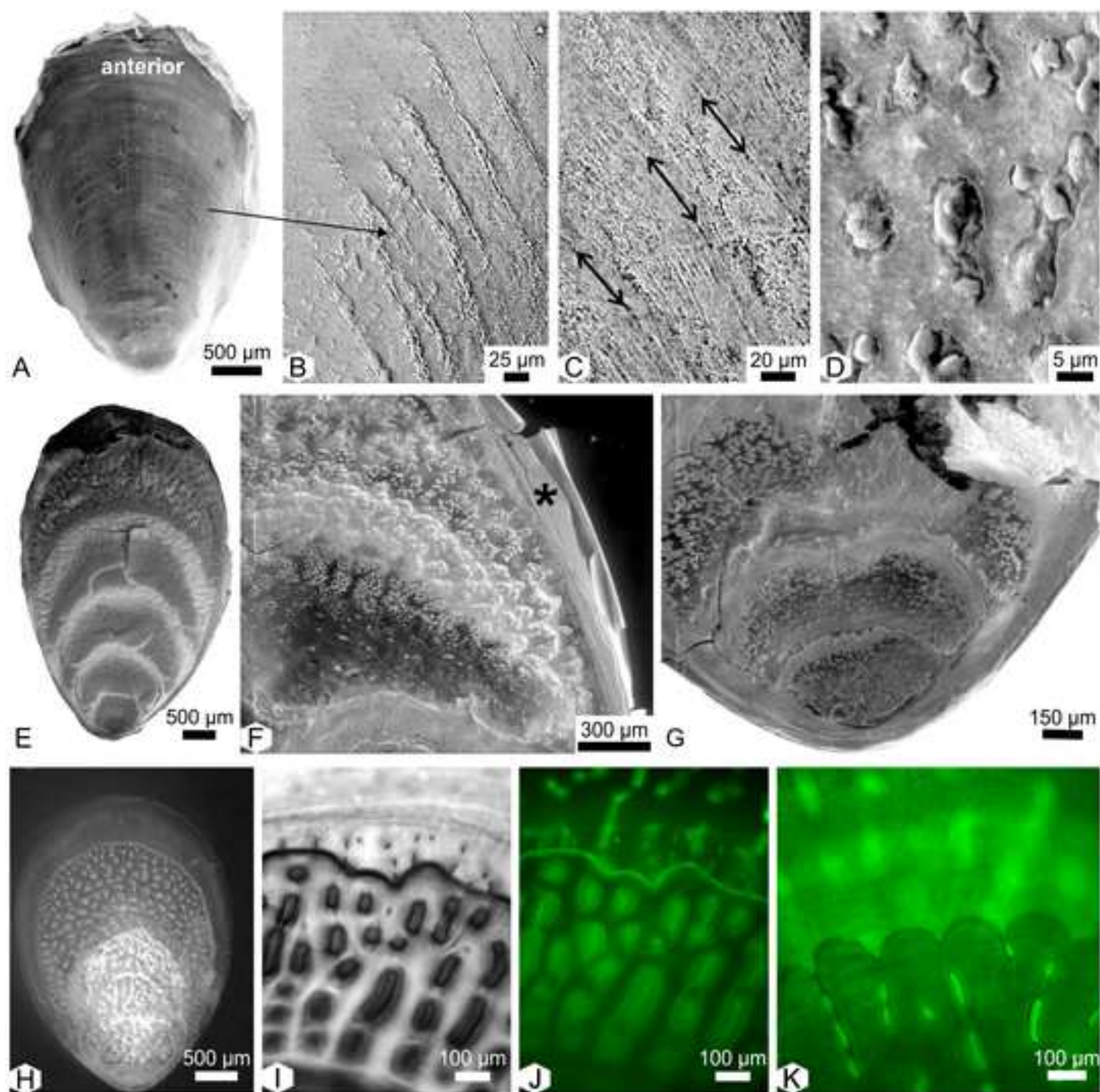
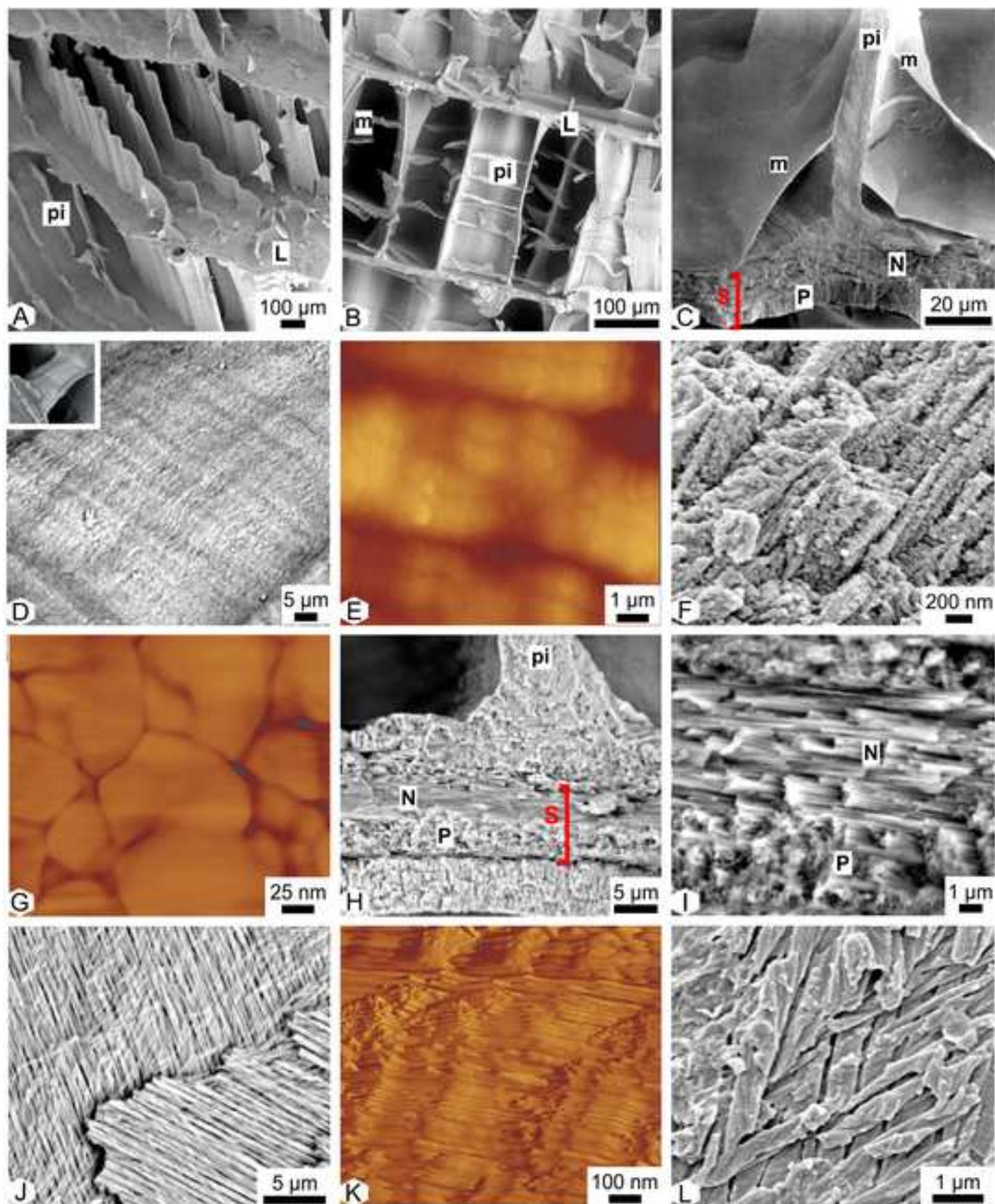
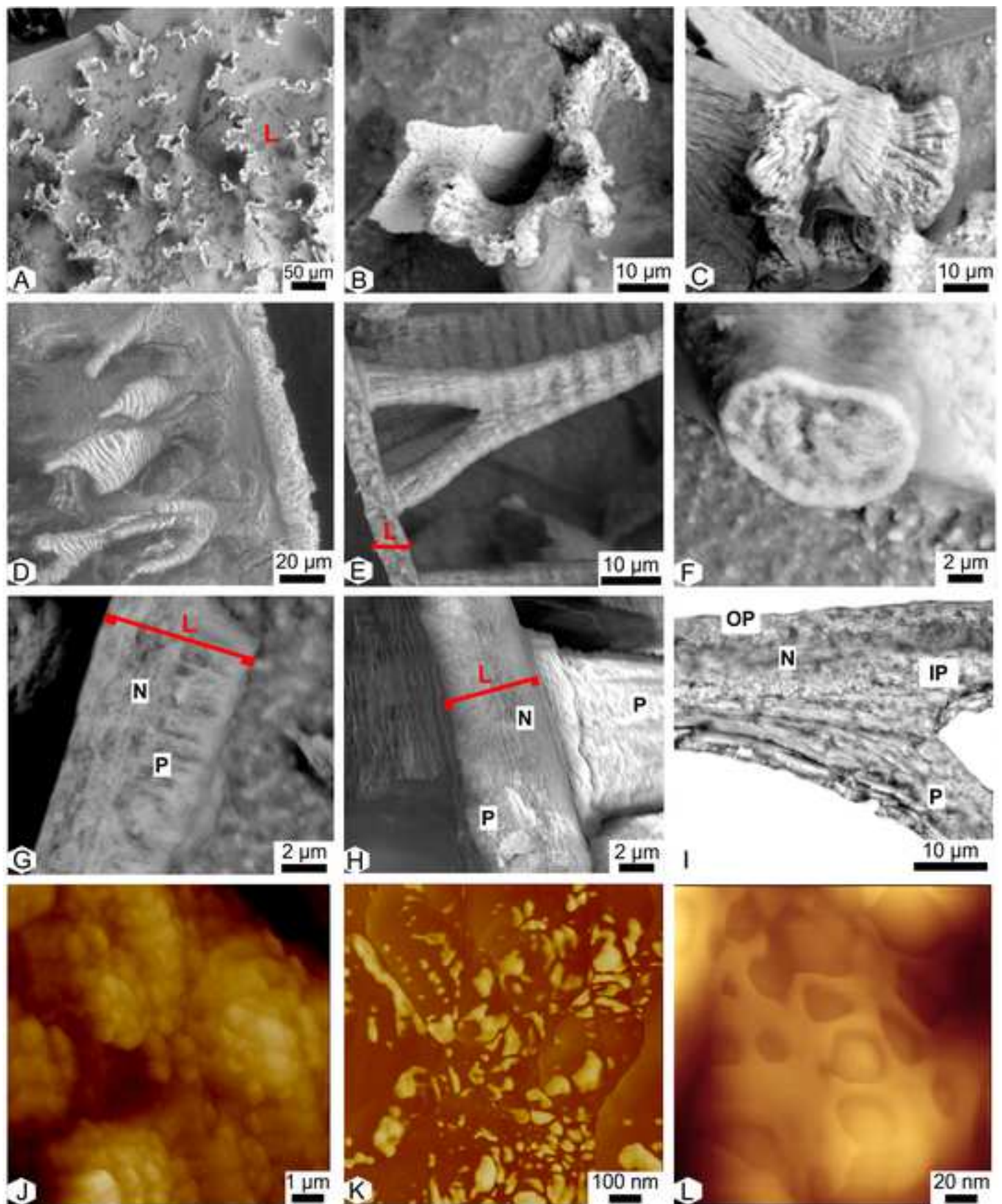
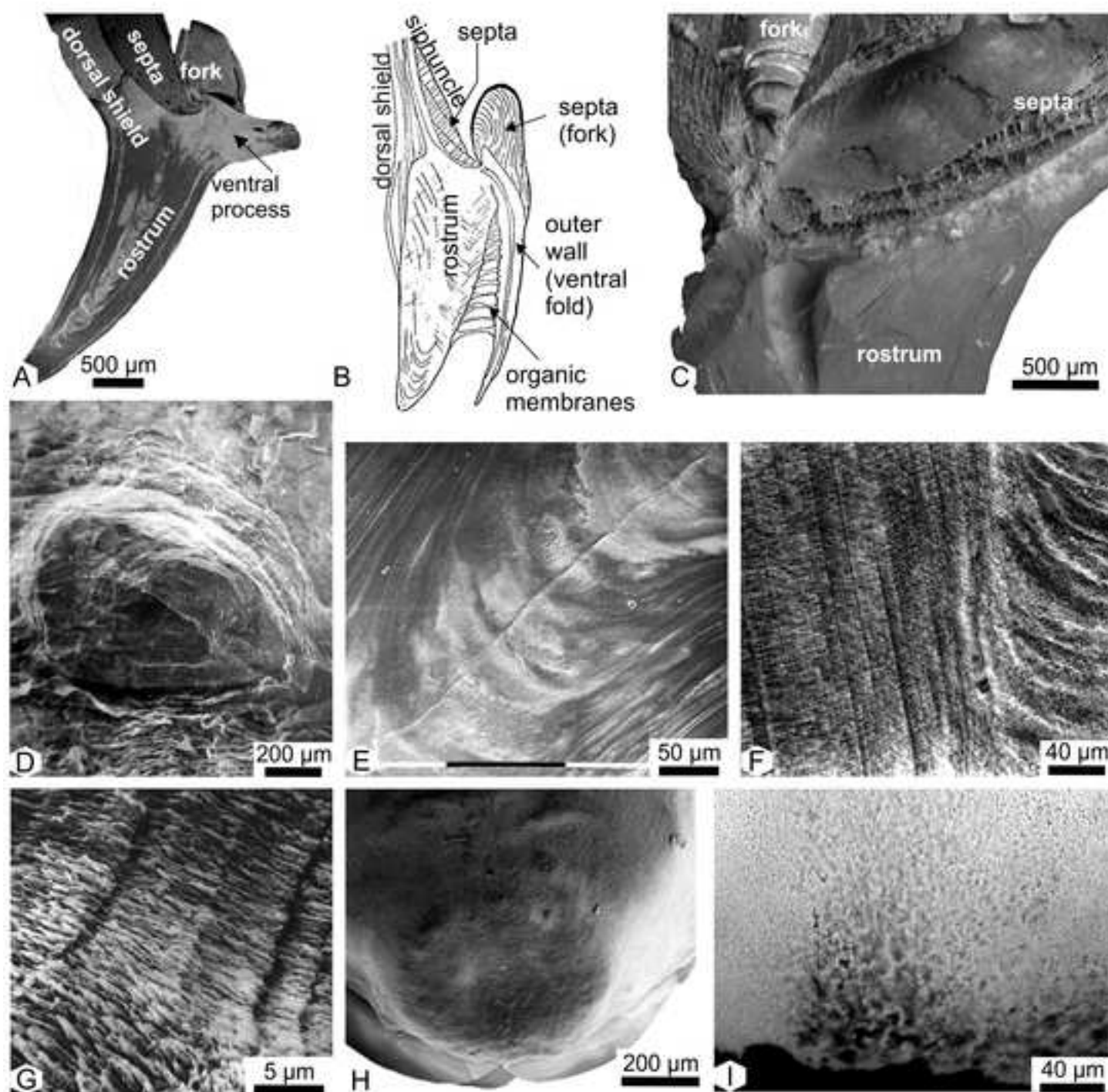
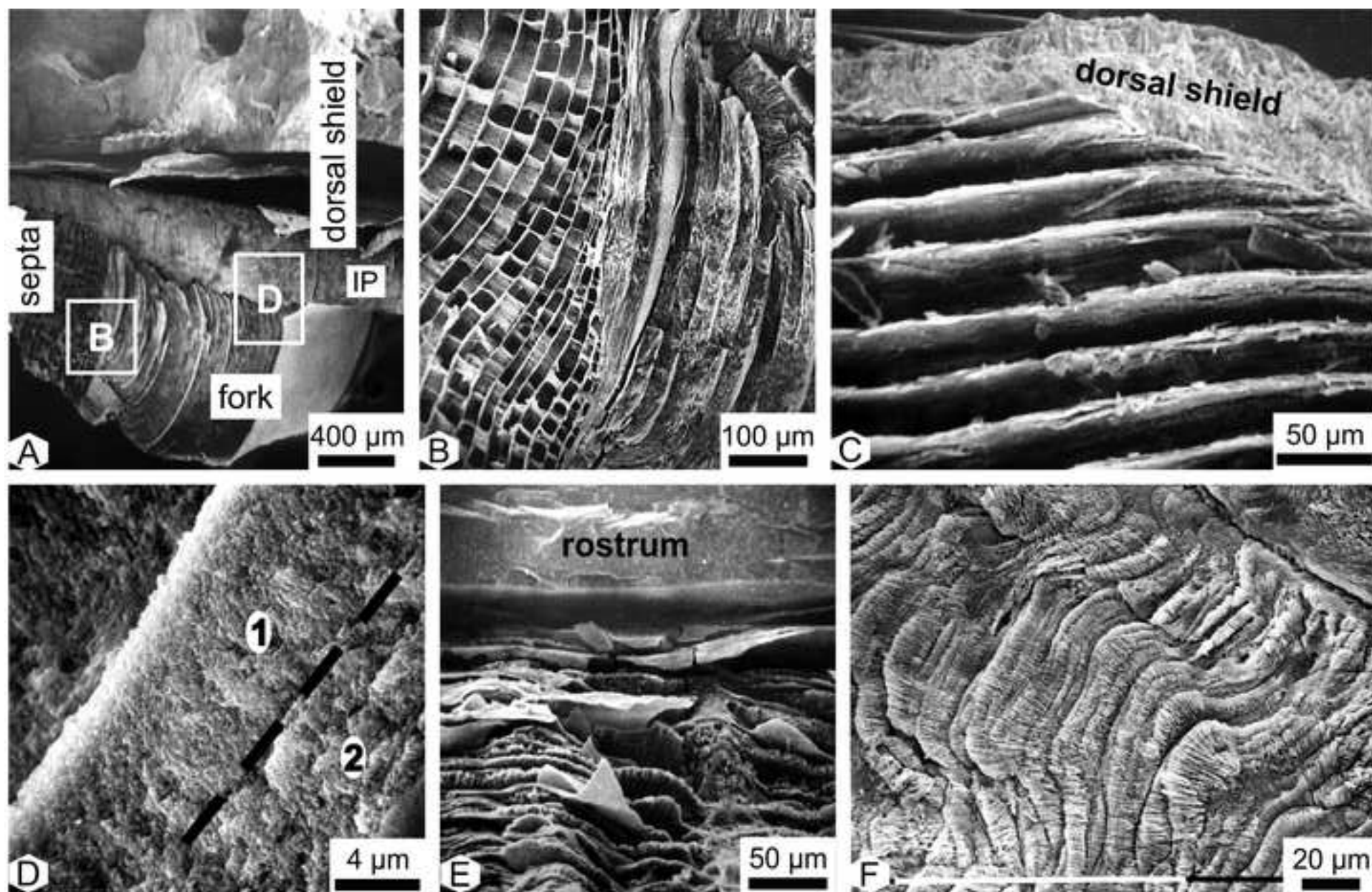


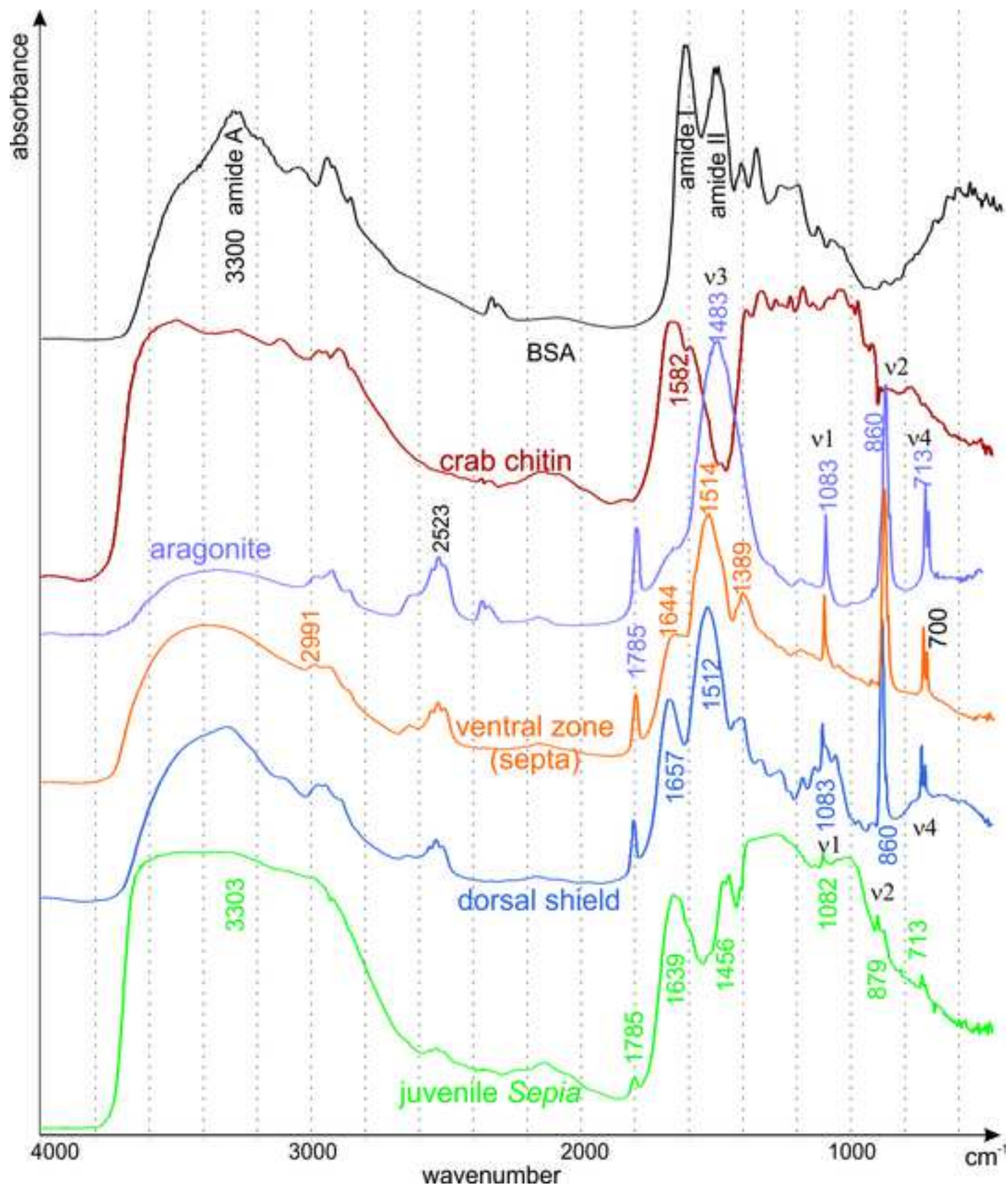
Figure 6

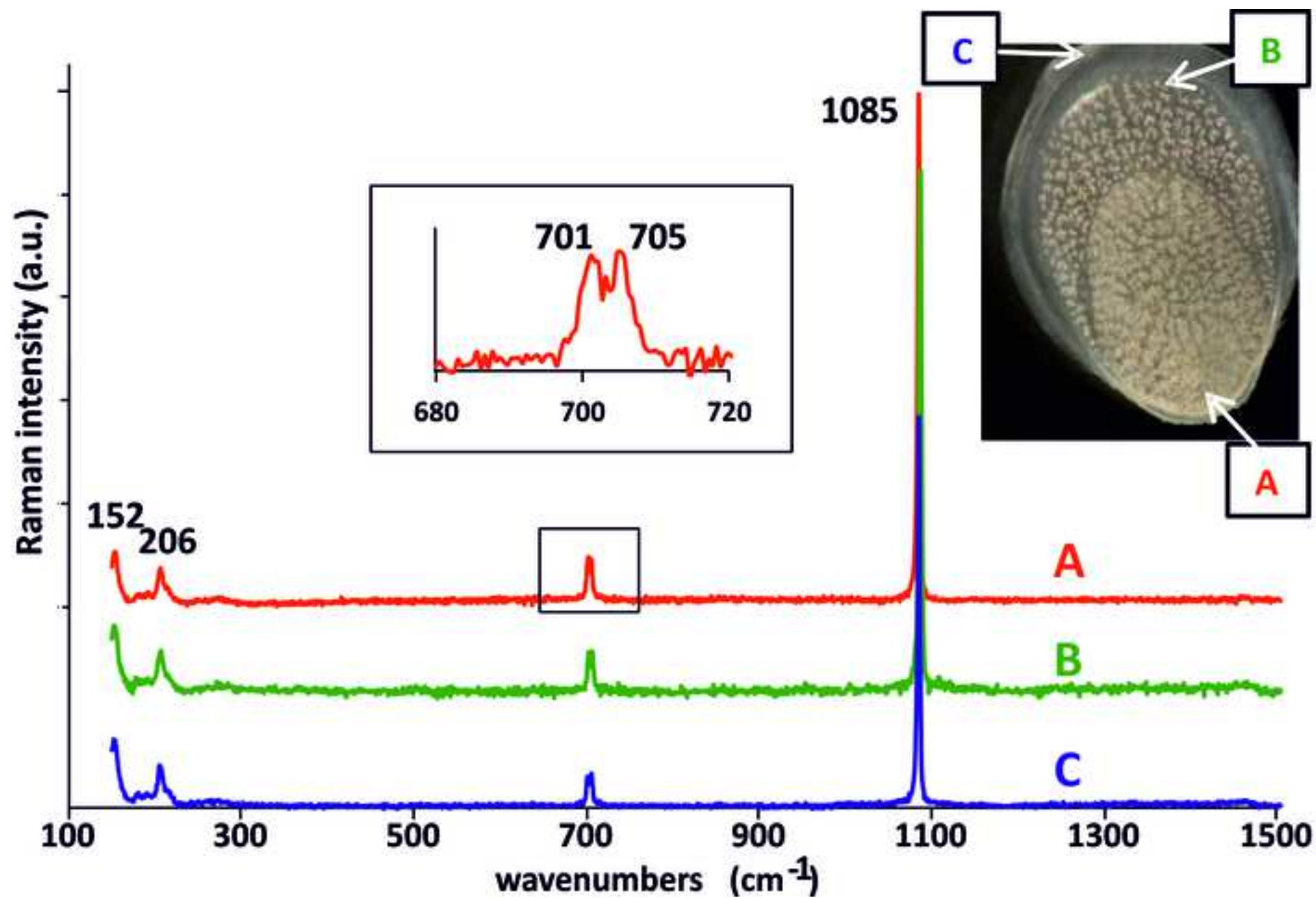












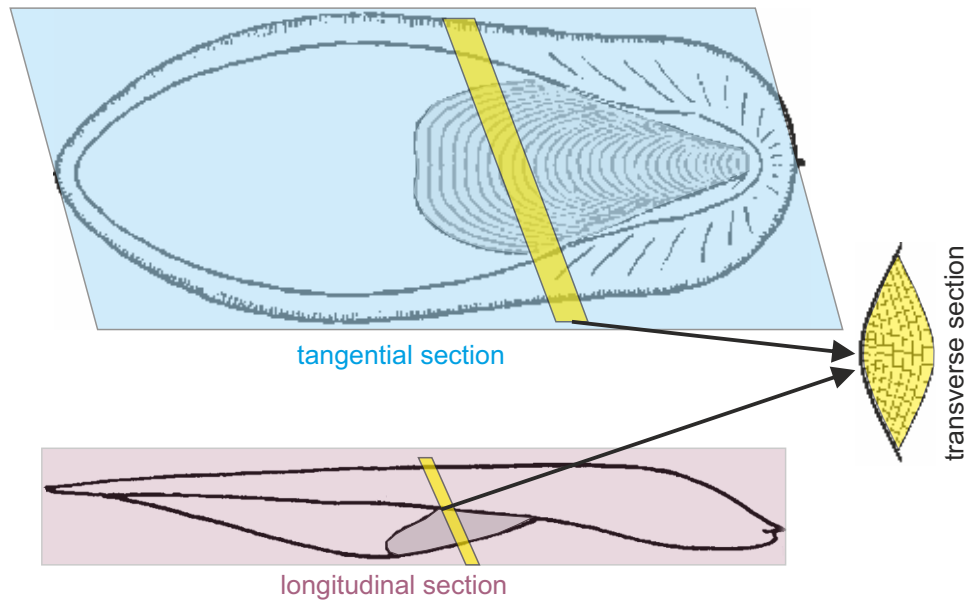


figure S1

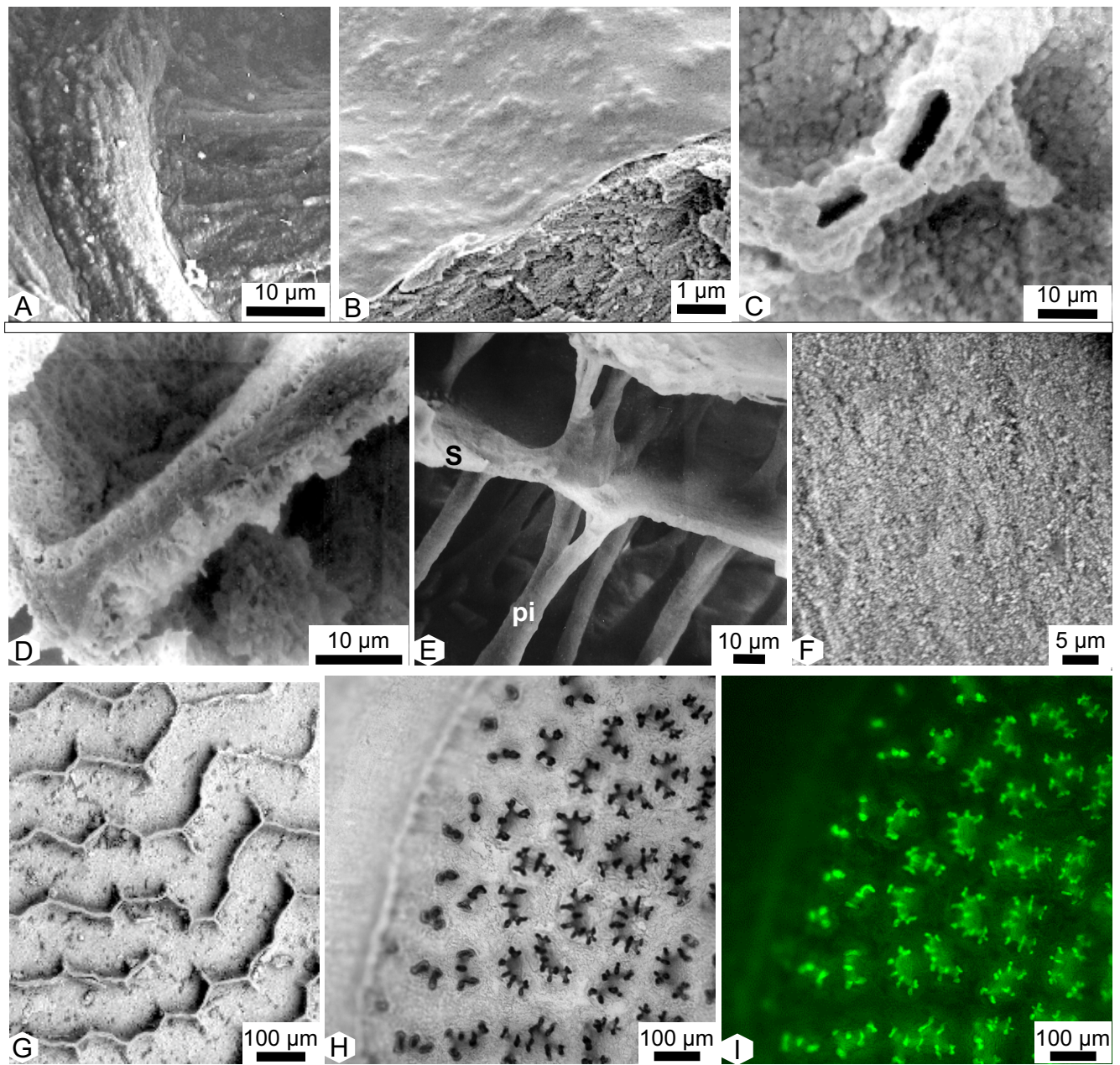


figure S2

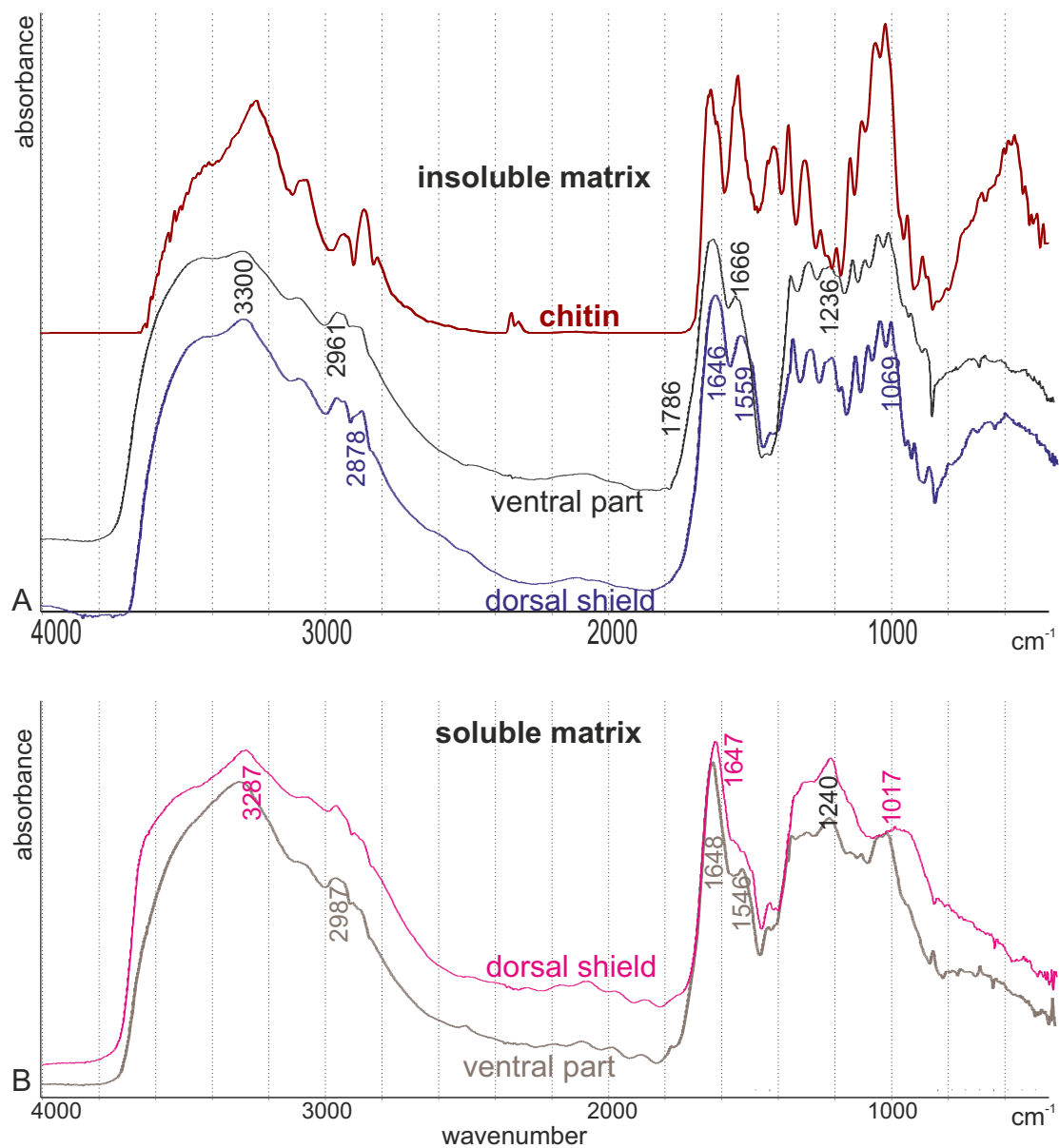


figure S3